# Image derived input function and motion correction for kinetic modeling of dynamic [18F] FET-PET/MRI for Gliomas

Master Thesis

For attainment of the academic degree of
**Master of Science in Engineering (MSc)**

in the Master Programme Digital Healthcare
at St. Pölten University of Applied Sciences

by
**Adriana Jukic, BSc**
dh211816

First advisor: Priv.-Doz. Dipl.-Ing. Ivo Rausch, PhD

[Vienna, 22.05.2024]

# Declaration of Honour

I hereby declare that

- I have written the work at hand on my own without help from others and I have used no other resources and tools than the ones acknowledged.
- I have complied with the Standards of good scientific practice in accordance with the St. Pölten UAS' Guidelines for Scientific Work when writing this work.
- I have neither published nor submitted the work at hand to another higher education institution for assessment or in any other form as examination work.

Regarding the use of generative artificial intelligence tools such as chatbots, image generators, programming applications, paraphrasing and translation tools, I declare that

☐ no generative artificial intelligence tools were used in the course of this work.

☒ I have used generative artificial intelligence tools to proof-read this work.

☐ I have used generative artificial intelligence tools to create parts of the content of this work. I certify that I have cited the original source of any generated content. The generative artificial intelligence tools that I used are acknowledged at the respective positions in the text.

Having read and understood the St. Pölten UAS‘ Guidelines for Scientific Work, I am aware of the consequences of a dishonest declaration.

# Preface

Creating this thesis was an incredible journey, filled with curiosity, determination, late nights, and the invaluable support of many people.

The idea for this work was inspired by my dear late friend, Peter Schaffarich. He helped me find a topic and supervisor. I am eternally grateful for his “pep talks.” He encouraged me to embrace academic challenges and always had faith in my abilities, often telling me, “Du schaffst das schon, Täubchen.”

I am deeply thankful to Ivo Rausch for his guidance, wisdom, and encouragement. He always listened to my ideas, even when they seemed far-fetched. Being under his supervision has been an honour. Thank you for being my supervisor.

My heartfelt appreciation goes to Iva Kopic, Nikolaus Irnstorfer, Stefan Witoszynsky, Christian Stejskal, Sabine Hasenbichler, Julia Kesselbacher, Philipp Haidegger, Sanel Alibegovic and Johannes Hardt. They all encouraged me, listened to me, helped me find solutions, and offered new perspectives. I couldn’t have finished this thesis without their kind words and patience.

At the beginning of this thesis, I was full of energy and excitement to explore the world of medical physics. A few months into the project, my motivation faded and frustration set in. Thanks to my sister, Betina Jukic, I never gave up. She always told me, “giving up is not an option, little girl.” Thank you for being there for me through this crazy journey, for your advice, and for reading my thesis even though it’s not your field.

Reflecting on the pages that follow, I remember the countless hours spent reading literature, conducting experiments, and trying to complete my thesis. Every moment of this academic journey has contributed to my growth and the development of the ideas presented.

A big thank you to Dejan Rasic whose late-night conversations and unmatched humor brought comfort and lightness during the toughest times.

My parents, Dubravka and Ivica Jukic, and brother, Adrian Jukic, were the main pillars of support. Their encouragement and understanding sustained me through the challenges of this academic pursuit. I am forever grateful for their faith in me.

This thesis would not have been possible without the help of my fellow researchers and colleagues.

# Abstract

Combined positron emission tomography (PET) – magnet resonance imaging (MRI) scans can be used in combination with the tracer O-(2-[18F] Fluoroethyl)-L-thyrosine (18F-FET) to dive deeper into the metabolic dynamics of gliomas. The clinical outcomes of gliomas are dictated by the specific type of tumor cells involved, such as astrocytes and oligodendroglial cells. Research initiatives are underway to enhance the diagnostic precision of prevalent imaging techniques, particularly PET/MRI scans. Despite the significance of this technique in diagnostics and treatment planning it faces a lot of challenges.

In order to achieve accurate diagnosis, it is important to quantifying the tracer uptake. The quantification process demands the measurement of the input function, indicating the cumulative availability of the radiotracer in arteries. Traditionally, this was achieved via arterial cannulation. However, a non- invasive approach utilizes an Image Derived Input Function (IDIF). Despite its advantages, this method faces complications due to the partial volume effects of the PET scanner's limited spatial resolution.

The primary objective of this thesis was to enhance a pharmacokinetic prototype for 18F-FET PET/MRI for gliomas by incorporating a quantitative accurate partial volume correction method, aiming to enhance the accuracy in kinetic modeling. This involved evaluating the time-sensitive activity concentration in the tissue near the carotid arteries. As a result, a spill-out and spill-in correction was developed that considers both time and tissue factors.

Patient movement during PET scans introduces artifacts and blurring, leading to inaccurate quantification of tracer distribution. To address the challenge of patient movement in PET imaging a motion correction alongside the IDIF was adapted.

The program underwent testing with a study group of 7 FET-PET/MRI patient data. For an effective comparison between the uncorrected and corrected IDIF the area under the curve, peak activity, paired t-test, and comparison with literature were utilized.

The developed IDIF provides quantitatively accurate representations of tracer concentrations over time for kinetic modeling. This confirms the potential to eliminate the need for invasive arterial blood sampling.

# Kurzfassung

Bei kombinierten Positronen-Emissions-Tomographie (PET)-Magnetresonanztomographie (MRT)-Scans wird vor allem der Tracer O-(2-[18F] Fluorethyl)-L-thyrosin (18F-FET) verwendet, um die Stoffwechseldynamik von Gliomen genauer zu untersuchen. Die klinischen Ergebnisse von Gliomen hängen von der spezifischen Art der Tumorzellen ab, wie z. B. Astrozyten und Oligodendrogliazellen. Derzeit laufen Forschungsinitiativen zur Verbesserung der diagnostischen Präzision der gängigen Bildgebungsverfahren, insbesondere der PET/MRI-Scans.

Um eine genaue Diagnose zu erhalten, ist es wichtig, den Tumor zu quantifizieren. Der Quantifizierungsprozess erfordert die Messung der Eingangsfunktion, die die kumulative Verfügbarkeit des Radionuklids in den Arterien angibt. Traditionell wurde dies durch eine arterielle Kanülierung erreicht. Ein modernerer und nicht-invasiverer Ansatz ist die Verwendung einer Eingangsfunktion. Trotz ihrer Vorteile ist diese Methode aufgrund des Partialvolumeneffekt und der begrenzten räumlichen Auflösung des PET-Scanners mit Komplikationen verbunden.

Das Ziel dieser Arbeit ist die Verbesserung eines pharmakokinetischen Prototyps für 18F-FET PET-MRT für Gliome. Durch die Einbeziehung einer quantitativen, genauen Methode zur Korrektur von Partialvolumeneffekten, um die Genauigkeit der kinetischen Modellierung zu erhöhen. Dazu wurde die zeitabhängige Aktivitätskonzentration im Gewebe in der Nähe der Karotis Arterien ausgewertet. Als Ergebnis wurde eine Spill-out-und -in Korrektur entwickelt, die sowohl Zeit- als auch Gewebefaktoren berücksichtigt.

Patientenbewegungen während PET-Scans führt zu Artefakten und Unschärfe was eine ungenaue Quantifizierung der Tracer-Verteilung zur Folge hat. Deswegen wurde neben der IDIF zusätzlich eine Bewegungskorrektur entwickelt.

Das Programm wurde mit einer Studiengruppe getestet, die aus 7 FET-PET-MRT-Patientendaten bestand. Für einen effektiven Vergleich zwischen der unkorrigierten und der korrigierten Eingangsfunkton wurde die Fläche unter der Kurve, die Spitzenaktivität, ein gepaarter t-Test und der vergleich mit der Literatur herangezogen. Die entwickelte Eingangsfunkton liefert eine quantitativ genaue darstellung der Tracerkonzentrationen im Zeitverlauf für die kinetische Modellierung.

# List of Abbreviations

| | |
|---|---|
| 11C-MET | 11C-methyl-methionine |
| 18F-FDG | 18 F-2-fluoro-2 deoxy-D-glucose |
| 18F-FET | 0-(2(18 Fluor)-Fluorethyl)-L-Thyrosin |
| 1p/19q-Codeletion | Loss of the short arm of chromosome1 and the long arm of chromosome 19 |
| 3D | Three dimensional |
| 4D | Four dimensional |
| APD | Avalanche Photodiodes |
| B1 | Gradient fiels |
| BGO | Bismuth Germanium Oxide |
| BLOD-fMRI | Blood oxygenation level dependent functional MRI |
| Bq | Becquerel |
| CNS | Central nervous system |
| DCE | Dynamic contrast enhanced |
| DICOM | Digital imaging and communication in Medicine |
| DWI | Diffusion weighted imaging |
| FALCON | Fast Algorithm for Motion Correction |
| FBP | Filtered back-projection |
| FLAIR | Fluid-attenuated inversion recovery |
| FWHM | Full width at half maximum |
| GE | General electronic |
| GSO | Gadolinium Orthosilicate |

| | |
|---|---|
| Gy | Gray |
| H | Hydrogen atoms |
| HF | High-frequency pulses |
| HU | Hounsfield units |
| ICA | Internal carotid artery |
| IDH | Isocitratdehydrogenase |
| IDIF | Image derived input function |
| J | Joule |
| keV | Kilo Electron Volt |
| LOR | Line of Response |
| LSO | Lutetium Orthosilicate |
| MLAA | Maximum Likelihood Expectation maximization |
| MR-AC | MR-based attenuation correction |
| MRI | Magnet resonance imaging |
| Mxy | Transverse magnetization |
| Mz | Longitudinal magnetization |
| NbTi | Niobium and titanium |
| NIFTI | Neuroimaging Informatics Technology Initiative |
| Ns | Nanosecond |
| OSEM | Ordered-Subsets Expectation maximization |
| PDF | Proton Density weighted |
| PET | Positron emission tomography |
| PMT | Photomultiplier-tube |

| | |
|---|---|
| PSF | Point spread function |
| PVC | Partial volume correction |
| PVE | Partial volume effect |
| ROI | Region of interest |
| SiPM | Silicon Photomultipliers |
| SSPDs | Solid-stat photo detectors |
| SSS | Single scatter simulation |
| SUV | Standardized uptake value |
| Sv | Sievert |
| T1W | T1 weighted |
| T2W | T2 weighted |
| TAC | Time activity curve |
| TE | Time to echo |
| TOF | Timet of flight |
| TR | Time of repetition |
| WB | Whole-body |
| WHO | Word health organization |
| α | Alpha |
| β | Beta |
| γ | Gamma |

# Table of Content

# 1 Introduction

Gliomas represent approximately 50% of primary brain tumors in adults. These tumors arise from glial, astrocytic, or oligodendroglial cells and vary in their aggression and clinical courses based on molecular markers. The survival rates span from 1.5 year to over a decade. Critical for patient management is the identification of specific biomarkers, notably the presence or absence of IDH gene mutations. The WHO 2021 classification separates astrocytomas from glioblastoma based on these mutations into IDH-mutant and IDH-wildtype categories. Additionally, diagnosing the prevalent oligodendroglioma requires the detection of 1p/19q codeletion combined with an IDH mutation [1].

Magnetic Resonance Imaging (MRI) stands as the foremost imaging technique for the initial evaluation and subsequent monitoring of gliomas. Yet, MRI encounters certain limitations in glioma management. Specifically, the contrast enhancement utilized for tumor assessment is non-specific, majorly reflecting disruptions in the blood-brain barrier. This disruption can result from various non-tumorous processes, including treatment-induced inflammation, postoperative alterations, seizure episodes, ischemia, radiation effects, and necrosis. Moreover, gliomas sometimes don't exhibit blood-brain barrier disruptions leading to MRI contrast enhancement, posing a challenge when examining low-grade gliomas or those with anaplastic elements. While non-enhancing tumor sections can be viewed on T2w- or FLAIR MRI, distinguishing between tumorous tissue and surrounding edema, ischemic damage, post-surgical modifications, or radiation impacts post-therapy can be challenging [2], [3].

Positron emission tomography (PET) scans with the tracer 18F-fluoroethyltyrosine (18F-FET) have been recognized as a valuable functional imaging technique, addressing certain MRI-based limitations in glioma diagnosis and monitoring. Particular, diagnostic methods that focus on quantifying tracer uptake behavior, represented as standardized uptake value (SUV) curves from dynamic PET scans, have been researched to differentiate between low and high-grade gliomas. Nonetheless, the underlying factors influencing observed tracer uptake remain elusive [4], [5].

To address these obstacles in 18F-FET PET studies, pharmacokinetic modeling of FET uptake is being explored [6], [7]. The distinct tracer uptake curves observed for various glioma grades suggest that FET uptake may follow unique kinetic models depending on the glioma type [4], [6].

To evaluate this hypothesis, an initial pilot study was conducted by Poglitsch [7] at the university hospital of Vienna. The software processes dynamic PET data and a contrast enhanced T1w MRI. It auto-generates a volume-of-interest to extract an image-derived input-function (IDIF) from the internal carotid artery using MRI data. Subsequently, it conducts pixel-wise modeling across the brain with four kinetic models and selects the best fit for each pixel.

## 1.1 Problem

Despite the significance of the 18F-FET-PET MRI in diagnostics and treatment planning it comes with a lot of challenges.

One of the challenges in achieving accurate diagnosis lies in quantifying the tracer uptake. The quantification process demands the measurement of the input function, indicating the cumulative availability of the radiotracer in arteries. Traditionally, this was achieved via arterial cannulation. However, a more contemporary and non- invasive approach utilizes an Image Derived Input Function (IDIF). Despite its advantages, this method faces complications due to the partial volume effects, a byproduct of the PET scanner's limited spatial resolution.

Another challenge is patient movement during the long PET/MRI scan, which can take up to an hour. Even minimal movement introduces motion artifacts between the frames which leads to misalignment of the region of interest (ROI). Since the ROI is the carotid artery, a very small and sensitive structure, any movement can cause significant shifts, compromising the accuracy of the imaging.

Poglitsch [7] has developed a pharmacokinetic prototype at the University Hospital of Vienna. By modeling the dynamic behavior of the 18F-FET tracer, this prototype offers a deeper understanding of tracer uptake dynamics in gliomas, allowing for more precise tumor analysis.

In order to increase the accuracy and expand the prototypes capabilities implementation of a motion correction and quantitative accurate IDIF are necessary.

## 1.2 Goal

To enhance the prototype's capabilities and accuracy, this thesis will focus on integrating a motion correction and partial volume correction. The primary objective of this thesis is to incorporate a quantitative accurate partial volume correction method, aiming to enhance the accuracy in kinetic modeling, especially when extracting the image- derived input-function. This will involve evaluating the time-sensitive activity concentration in the tissue near the carotid arteries. As a result, a spill-out and spill-in correction will be developed that considers both time and tissue factors. Ultimately, this thesis will deliver a motion correction and quantitatively accurate IDIF for effective kinetic modeling.

## 1.3 Main Hypothesis

1. The developed Image-Derived Input Function and motion correction can provide quantitatively accurate representations of tracer concentrations over time for kinetic modeling, eliminating the need for invasive arterial blood sampling.

## 1.4 Method and Structure

The data used for this thesis consists out of 7 retrospective FET-PET/MRI patient datasets which were used for the development of the kinetic modelling tool prototyped by Poglitsch. The study was approved by the ethics committee of the Medical University of Vienna, under code EK 1075/2020.

Poglitsch chose Python for his dissertation due to its open-source nature, strong community support, and extensive libraries, especially for image processing. This decision also influenced the use of Python to develop a simple motion correction and quantitatively accurate IDIF.

The objective of this thesis is to adapt and implement a motion correction alongside an accurately quantified IDIF. To evaluate its accuracy, the uncorrected IDIF will be compared with the corrected one.

To quantitatively assess the effectiveness of the implemented corrections two parameters and a paired t-test for statistical evaluation was conducted.

1. Area under the Curve

This metric is instrumental in quantifying the total trace concentration over time, offering a comprehensive view of the tracer's behavior within the region of interest.

2. Peak Activity:
   The peak activity identifies the highest tracer concentration observed, which is critical in assessing the success of the correction methods in enhancing the image quality.
3. Paired t-test:
   This statistical test will be used to compare the IDIF values before and after the application of corrections. It will help determine the statistical significance of the changes by the correction techniques.

Further Time-Activity-Curve graphs will be created to compare the corrected and uncorrected IDIF.

Since a ground truth, such as arterial blood sampling is missing the effectiveness of the PVC will be validated through a comparative analysis with existing literature.

# 2 Fundamentals

This thesis describes a special area of nuclear medicine and medical physics. In this chapter the medical, physical, and programming basics are explained.

## 2.1 Gliomas

Tumors of the Central Nervous System (CNS) are classified based on the cells from which they originate. For example, meningiomas develop from the brain's meninges, embryonic tumors from stem cells, hematolymphoid tumors from blood-forming cells, and gliomas from the brain's glial cells. Glial cells have various functions in the brain: amongst others they envelop nerve cells for structural support, electrical insulation, nerve cell sustenance, and play a role in forming the blood-brain barrier. Most glial cells in the CNS are astrocytes and oligodendrocytes, forming a complex network throughout the brain [1], [8].

Gliomas are the second most common primary brain tumors, with an incidence rate spanning from 6.6 to 10.5 per 100,000 people. “Glioma" refers to various types of malignant glial cell tumors, each with different levels of severity. These tumors can be classified into subtypes based on specific biomarkers, which indicate median survival rates ranging from 1.5 years to over a decade. [8].

An important factor in treatment decisions is identifying an IDH gene mutation. According to the WHO 2021 classification, the presence or absence of IDH1 and IDH2 gene mutations distinguishes astrocytomas from glioblastomas, classifying them as IDH-mutant and IDH-wildtype, respectively. For diagnosing oligodendrogliomas, it is essential to identify combined whole arm deletions of parts of chromosomes 1 and 19 (1p/19q codeletion) along with an IDH mutation [7], [9].

## 2.2 Nuclear medicine

Nuclear medicine is a specialized field that uses radioactive materials, known as radiopharmaceuticals or tracers, to diagnose and treat various diseases and conditions. It combines the disciplines of molecular biology, medical imaging, and nuclear physics to provide unique insights into the metabolic processes of organs and tissues. The advantage of nuclear medical imaging over radiological imaging

is that not only anatomical structures are visualized, but also metabolic processes of the body [10].

## 2.3 Tracer

More than 100 years ago, the foundation for modern tracer techniques was laid by the pioneering work of George de Hevesy, a Hungarian radiochemist. In the early 1920s, de Hevesy's experiments with radioactive isotopes marked a significant advancement in the field of chemistry and biology. Notably, in 1923, de Hevesy conducted a groundbreaking experiment involving the use of lead isotopes to study the absorption and transportation of lead in plant systems. He introduced a radioactive lead isotope into the nutrient solution of a plant and traced its movement throughout the plant's tissues. This experiment was seminal in illustrating the concept of using isotopes as tracers to follow the paths of substances in biological systems [11].

De Hevesy's work was not only instrumental in advancing the understanding of biological processes but also laid the groundwork for the tracer principle, a concept that revolutionized scientific research in many fields. The tracer principle involves introducing a small, detectable amount of a substance (the tracer), labeled with a radioactive isotope, into a system. By monitoring the tracer's behavior, scientists can derive valuable information about the dynamics of the system under study, such as metabolic pathways in organisms, the distribution of substances in the environment, or the functioning of complex industrial processes [11].

In the field of medicine, this principle led to the development of diagnostic techniques like Positron Emission Tomography (PET). PET scans use radiotracers to visualize and measure changes in metabolic processes, or physiological activities including blood flow, regional chemical composition, and absorption.

For his pioneering work in using isotopes as tracers to study chemical processes, especially in plants, George de Hevesy was awarded the Nobel Prize in Chemistry in 1943. His work not only provided a powerful tool for scientific research but also opened up new horizons in various fields, including medicine, environmental science, and biochemistry, leading to a deeper understanding of complex biological and chemical systems [11].

Today, molecules in which individual atoms are replaced by radioactive isotopes are used as tracers. The ionizing radiation, which is emitted by isotopes during decay, is measured and thereby the molecules are traced through the body. However, not all isotopes are equally suitable for these measurements. In order to

understand the selection of suitable isotopes the basic concepts of radioactivity are explained in the following section [12], [13].

Radioactivity is the act of emitting radiation spontaneously by an unstable atomic nucleus, which wants to give up energy in order to shift to a more stable configuration. A nucleus consists out of protons and neutrons. If there are too many neutrons in a nucleus it will emit a negative beta particle, which changes one of the neutrons into a proton. While if there are too many protons in a nucleus it will emit a positron changing a proton into a neutron [14], [15].

In certain scenarios, when a nucleus possesses excess energy, it may release this surplus in the form of a gamma ray. Gamma rays are high-energy photons that allow the nucleus to discard energy without altering its particle composition [15]. This process is typically observed in nuclei that are in an “excited state”, a condition where their internal components, such as protons and neutrons, possess energy levels higher than their most stable configuration. The emission of a gamma ray brings the nucleus from this excited state back to its ground state, where it has the lowest possible energy level.

In cases where a nucleus has an excess of mass, it may undergo alpha decay, emitting an alpha particle. An alpha particle is essentially a helium-4 nucleus, comprising two protons and two neutrons bound together. This emission occurs because protons, being positively charged, repel each other due to the electromagnetic force, one of the four fundamental forces in physics. The emission of the alpha particle, which is a relatively heavy entity compared to other forms of radioactive decay products, allows the original nucleus to reach a more stable, lower-energy state [14] [15].

However, because protons and neutrons are so closely packed together in the nucleus, they are held together by the strongest force the “strong nuclear interaction” (one of the four elementary forces). This creates a stable equilibrium [15].

Atomic nuclei, which have too many protons, too many neutrons or too much mass, are outside the equilibrium in an energetically too high and therefore unfavorable state. These nuclei can adopt an equilibrium state or at least approach it by releasing energy. There are several ways to do this, called different types of decay of an atomic nucleus, which release different types of radioactive radiation [14], [15].

α-radiation

*“Alpha radiation consists of alpha particles at high energy/speed. The production of alpha particles is termed alpha decay. Alpha particles consist of two protons and two neutrons bound together into a particle identical to a helium nucleus. Alpha particles are relatively large and carry a double positive charge. They are not very penetrating, and a piece of paper can stop them. They travel only a few centimeters but deposit all their energies along their short paths*.” [17].

β-radiation

Beta radiation consists of free electrons or positrons. Depending on the charge Beta radiation is distinguished between ß+ and ß- radiation. ß- decay is the electron emission, a neutron is converted into a proton, electron and antineutrino. The electron and antineutrino fly away from the nucleus, which now has one more proton. Since a proton is gained during ß- decay the atom changes form one element to another. Whereas during ß+ decay, which is also called the positron emission, a proton is converted into a neutron, positron and neutrino in the nucleus. The positron and neutrino fly away from the nucleus, which now has one less proton and the atom changes from one element to another. Both types of radiation can be shielded with thin aluminum [15], [18] [17].

γ-Radiation

Gamma rays are weightless packets of energy called photons; they are pure energy. The energy is reflected in the wavelength and thus in the frequency. The shorter the wavelength and the higher the frequency, the higher the energy of electromagnetic radiation. Gamma rays are often emitted during radioactive decay of alpha or beta particles. Furthermore, gamma radiation is produced during nuclear fission and fusion. Complete shielding is not possible it can only be attenuated with lead or other materials with high mass number [15], [18].

Ionizing radiation is not visible and cannot be registered by the human sense organs. The goal of dosimetry is to detect, measure and visualize radioactivity. The simplest measurement is the activity. It indicates the number of decay acts per second and its unit is 1 becquerel (1Bq) [15], [18].

However, since the different types of radiation transport different amounts of energy, a second measurement is defined: the dose. It is supposed to express the total effect of radiation on matter. The absorbed energy (in joules (J)) of a defined quantity of matter (in kilograms (kg)) is measured in grays (Gy), where 1 Gy = 1J/kg [16], [18].

Furthermore, since the absorbed dose doesn´t indicate any biological effect on the human body, a third measurand has been defined: the dose equivalent. This multiplies the absorbed dose by a quality factor (for γ- and β-radiation this is 1, for α-radiation 10) and is measured in the unit Sievert (Sv) [15], [18].

The radioactive decay of a single nucleus is unpredictable and spontaneous. Nevertheless, individual radioactive elements and isotopes differ in the average rate of radioactive decay. This can statistically be tangible with the half-life time of an isotope [14]–[16]. "T*he half-life of a radioactive isotope is the amount of time it takes for one-half of the radioactive isotope to decay*"[19].

For medical examinations special radioactive isotopes with neither a too long nor too short half-life time are used. Depending on the nuclear medical exam different isotopes are used, Positron Emission Tomography (PET) relies on ß+ emitters. [18].

The important positron-emitting isotopes for PET-scans are carbon-11, oxygen-15, fluorine-18 (18F) and gallium-68. For brain imaging amino acid-based tracers are widely used because they are sparsely taken up by healthy brain tissue but very well taken up by most malignant lesions in the brain. [11C- methyl]-methionine (11C-MET) and 18F-FET are the most used tracer for brain imaging [18], [20]–[22].

In the case of 18F-FET, the underlying amino acid has been deliberately modified so that it can be carried by the cell's competent transporter but is not incorporated into proteins [22].

## 2.4 Positron emission tomography

Positron Emission Tomography (PET) is an important imaging technique in nuclear medicine, designed for visualizing and quantifying biochemical and physiological processes using radioactive substances. During a PET scan, the individual is positioned within the scanner's field of view, after which the radiotracer is administered intravenously [16], [17].

The radiotracer's instability triggers its decay, leading to the simultaneous release of a positron. The released positron travels a specified distance, known as the "positron range," as it moves through the surrounding tissue. Eventually, as it slows down, the positron interacts with an electron in its path, to form a positronium.

Due to its inherently unstable nature, positronium undergoes self-annihilation, emitting two photons, each with an energy of 511 keV. These photons move in opposite directions. However, these annihilated photons are not perfectly collinear,

and this slight deviation can be attributed to the fundamental principle of conservation of momentum. This phenomenon happens because the positron, is not entirely at rest before it encounters the electron, leading to a minor misalignment in the emitted photons' trajectories. The fuoundation of PET imaging relies on the principle of coincidence detection, wherein these annihilated photons are detected [18].

### 2.4.1 PET-imaging

As established above PET imaging operates on the foundational principle of coincidence detection, as shown in Figure 1. The architecture of the PET system is characterized by a cylindrical configuration of detector rings. These rings produce timed pulses upon the detection of annihilated photons [18], [16].

Conventional PET detectors utilize scintillation crystals such as Bismuth Germanium Oxide (BGO), Gadolinium Orthosilicate (GSO), and Lutetium Orthosilicate (LSO), which are seamlessly integrated with Photomultiplier Tubes (PMTs). When incident photons interact with these scintillating materials, they induce fluorescence. This fluorescence is subsequently transformed into electrical pulses by the PMTs. These derived pulses are then relayed to the coincidence circuitry. Photon pairs producing timed pulses within a predetermined temporal bracket (typically ranging from 6-12 ns) are deemed coincidental. Every coincidental event related to a photon pair is allocated a Line of Response (LOR) that seamlessly links the respective detector pair. This LOR provides the position of the annihilation, suggesting that the annihilation incident occurred somewhere along its trajectory [16].

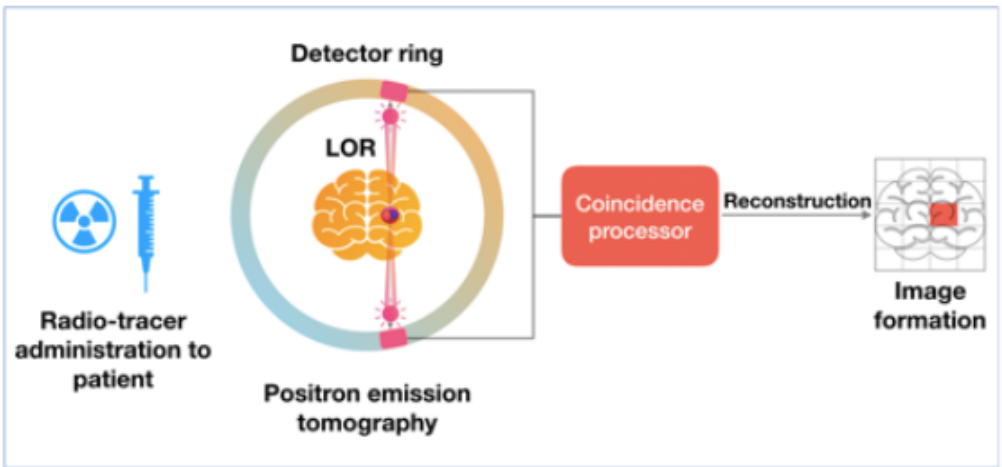


Figure 1: PET image formation. This image has been adapted from Sundar [19]

Figure 1 shows a simplified outline of the PET image creation process. The patient receives the radiotracer, which is then followed by data collection. Detector pairs identify the annihilation photons, and these are deemed coincidental if they are within a specific timing window. The gathered data is preserved either as a sinogram or in list-mode before it's reconstructed to produce the PET images.

Coincidence occurrences are classified into three categories: true coincidences, random coincidences, and scattered coincidences. For the latter two categories, the provided positional data of the annihilation event is incorrect due to the misalignment in the LOR. The primary factor for this discrepancy arises from the interactions of the annihilated photons with the surrounding biological tissues [16].

PET data can be classified into two main categories: sinograms and list-mode data, visualizing multiple LORs emerging from one single point within a subject.

If these LORs are graphically represented based on their orientation (y-axis) and their minimal displacement from the gantry center (x-axis), the resulting diagram would show a sinusoidal pattern. By doing this process for every point within a single plane of the subject, one can generate a sinogram. These derived sinograms are then processed further to yield three-dimensional PET visualizations [16].

In the context of list-mode data acquisition, every identified coincidence event is stored in a structured format. This format carries a range of specific information: the event type, the exact coordinates of the detector pair, the energy of the captured photon pair, along with temporal data etc. It's essential to note that list-mode data offers enhanced spatio-temporal fidelity [16], [20].

After acquiring the coincidence events, specialized reconstruction algorithms are used to create an image showing the radiotracer's spatial distribution within the scanned subject. These image reconstruction methods are divided into two types: analytical and iterative [16] .

Filtered back-projection (FBP) is a common analytical technique. It reconstructs the tracer distribution by performing an inverse Radon transformation on the projection data. To improve the image quality, a high-pass filter is integrated to elevate the visual quality of the reconstructed image. However, the filtration process can increase the noise in the images [21].

The iterative approach offers a more detailed representation of the system. Typically, these methods involve repeating a series of steps until specific convergence criteria are reached [21]. First, the raw dataset is created from an initial image based on the PET system´s model. This generated data is then

compared with actual data obtained from the system. The result of this comparison produces calibration factors which are vital for fine-tuning the raw dataset. Among iterative techniques, the Maximum Likelihood Expectation Maximization (MLEM) [22] and its advanced version, the Ordered-Subsets Expectation Maximization (OSEM) algorithm [23], are the most well-known methods. MLEM's aims to create an accurate image by iteratively comparing the correlation between estimated and actual acquired projections. Due to its structure, which requires multiple iterations to reach an optimal solution, MLEM can be time- consuming. In contrast, OSEM, an accelerated version of MLEM, optimizes this process. It groups angular projections into specific subsets, applying the MLEM methodology to the entire subset instead of each projection. This streamlined approach not only reduces computational time but also OSEM's has similar quantitative accuracy to FBP [21], [24].

### 2.4.2 Data correction

The data obtained from PET imaging is influenced by various factors that compromise both its qualitative and quantitative information. Influences such as discrepancies in detector efficiencies across detector pairs, photon attenuation, and the incidence of random and scatter coincidences affect the acquired data. An assessment and adjustment for each of these factors is important prior to the data reconstruction. A detailed overview of these components and their associated corrective measures is provided in the following chapter.

### 2.4.3 Normalization

Within the context of normalization, it's crucial to understand that PET systems are composed of many detectors grouped into blocks. These blocks are then connected to a multitude of photomultiplier tubes (PMTs). Variations in efficiency among detector pairs arise from multiple sources, including the detector's placement within its block, physical characteristics of the detectors, and the gain adjustments of the related PMTs. Such variations lead to data non-uniformities. To address these inconsistencies, a normalization process is executed [25]. This is performed by exposing all detector pairs to a 511 keV photon source, such as a 68Ge source, which is strategically positioned within the field-of-view. The collected data is used to determine normalization factors for each detector pair. This determination is based on the ratio of the overall average count from all pairs (LORs) to the count from an individual detector pair. These calculated normalization factors are then applied to the corresponding data sets in the patient's sinogram [16].

### 2.4.4 Attenuation Correction

As photons resulting from annihilation events pass through the tissue of a subject, they are attenuated. The extent of this attenuation is depending on factors such as the tissues thickness and tissue components. This leads to an observable decrease in the detected photons across each LOR. To preserve the quantitative accuracy of PET images, it important to account for these attenuation effects [26]. In traditional standalone PET systems, the calculation of attenuation coefficients for each LOR is done by a rotating transmission source [27]. The process involves performing two scans using the rotating source: an unobstructed blank scan and a transmission scan with the subject positioned within the field of view. By dividing the blank scan with the transmission scan the attenuation coefficients are calculated, which are then used to adjust each specific LOR for attenuation effects.

In state-of-the-art PET/CT configurations, the CT transmission image is seamlessly converted into an attenuation profile via tube-voltage-dependent bilinear transformation processes [28], [29]. Creating an attenuation profile directly from MR images, in fully integrated PET/MRI scanners, presents a unique challenge. This complexity arises from the lack of a straightforward connection between MRI signals and the attenuation characteristics of tissue. However, innovative methodologies [30] have been created and verified, with a special focus on cerebral studies [31].

### 2.4.5 Scatter Correction

The photons resulting from annihilation events may be exposed to Compton scattering on their way through the subject´s tissue. An important point is that the detectors themselves could induce scattering which would lead to a change in the trajectory of these photons [32].

As a result, the LOR for scattered photons may not accurately represent the genuine location of the annihilation event (refer to Figure 2). The scattering phenomenon significantly influences the ultimate image quality, affecting not only quantitative parameters but also qualitative characteristics. This is particularly noticeable as it reduces the contrast in the resulting reconstructed images. Among the various techniques used for scatter correction in both PET-CT and PET-MR systems, the Single Scatter Simulation (SSS) method takes a prominent position [33], [34].

This algorithm is based on the assumption that only one of the two annihilation photons is undergoes to Compton scattering. By using an estimated activity distribution, the medium's attenuation properties, the physical model of Compton

scattering, and the SSS method estimates the scatter distribution. The scatter sinogram derived from the SSS model is then subtracted from the originally measured sinogram prior to the process of image reconstruction [33].

### 2.4.6 Random Event Correction

Random events occure when two unrelated 511 keV photons (originating from different annihilation processes) are simultaneously detected by a pair of detectors within the intended coincidence time frame (as in Figure 2). Such events lead to an inaccurate LOR, which does not accurately reflect the actual position of the annihilation event. These random events have a negative effect on the quality of the reconstructed images, most notably reducing image contrast. To counteract and correct these random events, a dual coincidence circuitry system was implemented: the primary mechanism works within the conventional time frame, while a secondary system operates within an extended time window. Both systems maintain the same energy window parameters. The primary mechanism records a mix of random and true events, while the extended system records only the random events [16]. During the correction process, the counts from the extended window are subtracted from the conventional window's counts, resulting in a refined count of true coincidence events [16], [25].

Figure 2 shows true, scatter and random events. A 'true event' captures two photons from the same annihilation point without any scatter or attenuation interference. For 'scattered events', at least one of the photons deviates from its initial path due to scattering. A 'random event' involves detecting two photons from separate positron annihilations that occur within the coincidence timing window [19].

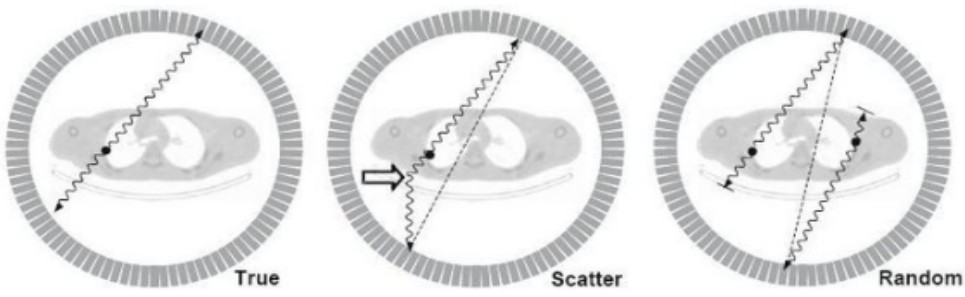


Figure 2: Types of coincidences [34]

## 2.5 Partial Volume effect

The partial volume effect (PVE) occurs due to the limited spatial resolution of the PET systems. This effect has quantitative and qualitative impacts on PET images especially when examining the IDIF of the brain. One of the reasons is that the diameter of arteries is close in size to the full-width-half maximum of the PET scanner. Essentially, PVE arises primarily because of two different reasons: [26], [35]

- Limited spatial resolution
- Discrete image sampling of a continuous 3D activity distribution

The Partial Volume Effect is responsible for the spreading of radiotracer activity, causing it to spread not only within the primary region of interest but also into the neighboring anatomical structures, and vice versa. This effect results in a blurring or smearing of the observed activity distribution. Such smearing can lead to significant discrepancies in the PET quantification, potentially resulting in either underestimations or overestimations of true radiotracer concentration. To address these discrepancies, various partial volume correction (PVC) methods have been proposed. These methods primarily utilize anatomical insights derived from co-registered CT or MR imaging to improve the accuracy of PET imaging results [36]-[37].

PVC techniques can be separated into two primary classifications post-reconstruction and reconstruction-base PVC methods. Prominent post-reconstruction PVC techniques are:

- Recovery Coefficient Correction
- Müller-Gärtner methodology
- Geometric Transfer Matrix

These techniques require an in-depth understanding of the system's structural parameters and its point-spread function for effective PVC execution. Typically, the point-spread function is conceptualized as a spatially-consistent isotropic 3D Gaussian function, the full-width-half-maximum (FWHM) which mirrors the system's spatial resolution [38]. Reconstruction-based methodologies improve spatial resolution by encapsulating partial volume influences via system-response modeling [39].

### 2.5.1 Spill in and out correction

Central to addressing the Partial Volume Effect in PET imaging is the correction for spill-in and spill-out effects, which are direct consequences of PVE.

Spill-in happens when radioactivity from outside a particular region of interest (ROI) enters into that ROI due to the PET system's limited spatial resolution. To illustrate, if an area with high radioactivity is adjacent to one with lower activity, the increased activity can seem to "leak" into the less active zone, resulting in overestimated activity levels for the latter [40], [41].

Conversely, spill-out describes situations where the radioactivity within an ROI appears to extend beyond its boundaries, again due to the system's limited spatial resolution. This means that some activity from the ROI appears to spill-out into nearby tissue areas, causing an underestimation of the actual activity within the ROI [40], [41].

For accurate quantification of PET-data it is crucial to address these phenomena. Correction for spill-in and spill-out are designed to reflect the true trace uptake more accurately in the ROI by adjusting the measured activity concentrations [41].

In the paper of Sundar's et al. "*Towards quantitative [18F]FDG-PET/MRI of the brain: Automated MR-driven calculation of an image-derived input function for the non-invasive determination of cerebral glucose metabolic rates."* The authors developed an enhanced spillover correction to achieve a quantitative IDIF [42].

The primary steps in their correction process involved addressing the background activity in the target region (known as spill-in) and subsequently correcting the loss of actual activity within the designated area (spill-out). Effective implementation of these corrections requires an understanding of both the system's point spread function (PSF) and the distribution of background activity [42].

In their study the PSF was determined using a 1-mL syringe filled with [18F]FDG, placed similarly to the presumed internal carotid artery (ICA) position. After processing and comparing data, the full width at half maximum (FWHM) of the PSF for the system was determined to be (6.0 ± 0.4) mm [42].

For an accurate assessment of background activity, they defined a spill-out zone based on the derived PSF. An initial background zone was determined to be 10mm away from this area's edges. Recognizing variations in background activity, the region was divided into 20 segments. Through a series of computations, adjustments were made to ensure uniformity of the tracer concentration and to account for radial differences. The final ICA value accounted for these

irregularities. This iterative process was applied to all PET frames, resulting in a corrected image-derived input function [42].

Accurate quantification of PET data is crucial for both diagnosis and therapy evaluation. 18F-FET PET/MRI scans are acquired dynamically to capture the kinetics of the trace uptake over time. The IDIF provides essential data for modeling the dynamic of the radioactive tracer in the brain. Unfortunately, the IDIF is compromised by spill-in and spill-out effects [43].

### 2.5.1 Image derived input function

The tracer concentration in the blood is referred to as "input function." It's an external component in the pharmacokinetic modeling, which is predetermined and remains unaffected when resolving differential equations [36]. This function describes the temporal variation in blood activity during an examination. To determine this concentration, continuous invasive measurements are required during the examination. While it's assumed the activity in the blood is homogeneously distributed, discrepancies can arise shortly after the tracer's application. Due to its invasive nature and the potential risks, this method is not commonly used [36].

Multiple methodologies to determine an input function have been developed as alternatives. A more practical and well-researched method is to derive the input function from the dynamic PET scan itself. This means assessing the activity in major blood vessels, then using this activity's temporal trajectory as the input function. However, inaccurately pinpointing the location of these vessels can lead to errors. In the beginning stages of the scan more accurate values are obtained when vessels are used to create the input function, especially those that supply the area being examined [36], [42].

## 2.6 Motion correction

During PET/MRI neuroimaging sessions, managing both involuntary and voluntary motion is crucial. Involuntary movements, such as breathing and heartbeat, occur naturally and are beyond the patient's control. While, voluntary movements arise from discomfort or a need for the patient to adjust their position. These movements can create motion artifacts, distortion of images and decrease the accuracy of PET's quantitative analysis [44].

Several solutions have emerged to counteract these motion artifacts. Hardware strategies, for instance, involve placing optical markers on the patient's head to

track motion throughout the scan. Data-centric techniques divide the scan into short time segments, realigning them to correct any motion-related distortions. The integration of PET and MRI technology further introduces MR-assisted methods, which can be hardware, image, or navigator-based [44], [45], [46].

Sundar et al. developed with his research group the “Fast Algorithm for Motion Correction” (FALCON) software. It offers a solution to correct both fixed and flexible motion distortions in dynamic whole-body (WB) images, regardless of the PET-CT system or tracer used. This correction is achieved through an initial affine alignment, followed by a diffeomorphic method to address flexible deformations, with images aligned at multiple scales. The software auto-determines suitable frames for efficient motion correction using an initial normalized cross-correlation metric. Testing across three PET-CT systems using six different tracers showed a significant reduction in motion-related errors. Notably, body motion artifacts were reduced by 50%, liver motion was entirely corrected in roughly 70% of cases, and tumor clarity was enhanced, increasing average tumor SUVs by 15%. Moreover, large deformations in specific cardiac images were addressed without creating further image distortions. The consistency in concentration levels of activity was maintained in large organs, with less than a 2% change pre and post-correction.

In summary, FALCON provides a quick and precise solution to correct motion-related issues in medical images, making it versatile for various PET imaging contexts [46].

Miranda et al. [47] focused in a study on improving rigid motion correction in PET imaging by enhancing the accuracy of motion tracking data. The researchers developed a method to correct marker displacement over the skull and small residual translation tracking errors. Using [18F]FDG and [18F]SynVesT-1 scans in awake mice and rats, they demonstrated that these corrections significantly improved image contrast and quality. The improvements were measured by the Image Enhancement Metric (IEM), showing notable increases in image contrast after applying the corrections, indicating better motion-corrected reconstructions [47].

## 2.7 Magnet resonance imaging

Magnetic resonance imaging is an imaging technique that produces cross-sectional images of the human body in different planes (coronal, sagittal and axial). It's crucial to emphasize that MRI operates without ionizing radiation. Instead, it relies on the manipulation of magnetic fields and the application of high-frequency

pulses to stimulate hydrogen atoms (H) within the body. Additionally, the remarkable soft tissue contrast offered by MRI sets it apart as a valuable imaging modality when compared to other techniques [48].

The magnetic field of an MRI scanner is always upright because the superconducting electromagnet conducts the electric current without resistance, it remains endless in the coil (made of niobium and titanium (NbTi)). The superconductivity of a magnet results from the fact that current is induced once and the system is cooled by liquid helium to -269°C (near absolute zero temperature). At this temperature, the coil loses its electrical resistance and conducts the current endlessly [48].

Hydrogen atoms are stimulated by magnetic fields and high-frequency pulses. An important property of the H is the intrinsic angular momentum about its own axis, the so-called nuclear spin. Under normal circumstances, the orientation of the H is in any direction. When the hydrogen atoms are introduced into a magnetic field, two special features occur, precession and longitudinal magnetization. In precession, the H gyrate (at the Larmor frequency), in addition to the nuclear spin, along the magnetic field axis. Longitudinal magnetization causes the hydrogen atoms to align in the magnetic field direction. Some of the H align parallel and some antiparallel to the field, the stronger the magnetic field the more H align parallel. The small excess of parallel aligned hydrogen atoms is called net magnetization and is the basis for the MRI images [49].

To explain the physical processes involved in MRI imaging more clearly, the axes are described using a coordinate system.

- z-axis = main magnetic field direction B0, longitudinal magnetization Mz (patient position)
- x-axis = horizontal axis, transverse magnetization Mxy
- y-axis = vertical axis, transverse magnetization Mxy

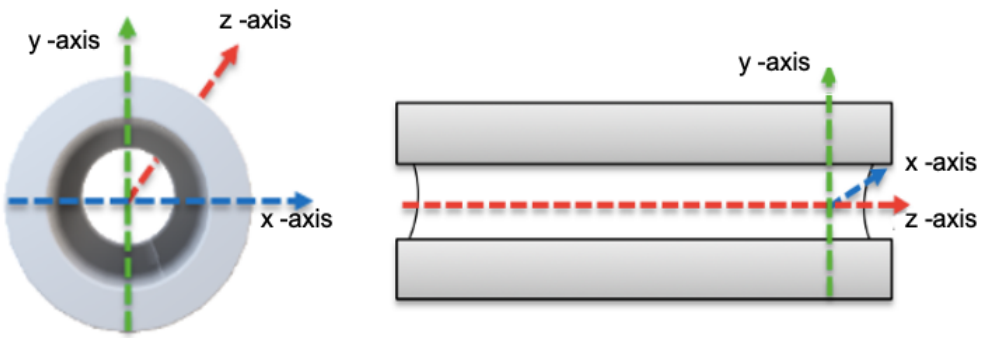

Figure 3: MRI cross section and longitudinal section showing the axes

To obtain the required signal for MRI, the hydrogen atoms must be shifted to a higher energy. Through high-frequency pulses (HF) energy is supplied to the H as long as the pulse is transmitted. The HF must have the same Larmor frequency with which the hydrogen atoms precise along the magnetic field axis. This leads to the phenomenon "resonance." Due to the HF, the H are transferred from the longitudinal magnetization (Mz) to the transverse magnetization (Mxy) and are synchronized. When the hydrogen atoms are synchronized, all H are forced to the same position in the gyroscopic motion. During the duration of the high- frequency pulse, there is a decay of the longitudinal magnetization with a simultaneous buildup of the transverse magnetization and phase alignment of the hydrogen atoms. When the radio frequency pulse is switched off, the energy release, during the relaxation of the hydrogen atoms, produces the MRI signal. While the relaxation phase is in progress, longitudinal magnetization is restored (T1 relaxation) and dephasing of the H occurs (T2 relaxation). The signal depends on the magnetic field, proton density, T1 relaxation time and T2 relaxation time. The proton density, T1 and T2 relaxation depend on the tissue and from this the different contrasts for MRI imaging can be generated [49], [2].

In order to generate an image from the resulting MRI signal, the position of the H in the spatial planes z, x and y must be encoded, the so-called spatial encoding. For this, the gradient coils located around the main magnet are needed.

Layer position and thickness are encoded via the layer selection gradient and the other two spatial planes are determined by the phase and Frequency encoding gradients. The layer coding is done by selecting the plane and cannot be swapped, phase and frequency coding direction can be swapped with each other [2].

If current is applied to the gradient coils another magnetic field is induced (B1 = gradient field). This B1 is superimposed on the B0 and can be changed in a targeted manner. At one end of the gradient the main magnetic field is strengthened and at the other end it is weakened. The Larmor frequency of the H is also changed, so only the H defined by a certain frequency interval are stimulated. By switching on all three gradients in coordinated manner, an exact location definition of the hydrogen atoms is possible [2].

Figure 4 shows B1 and how a layer is selected. By means of the frequency intervals and the triangle it is shown that the B0 is amplified on the right and weakened on the left by the B1.

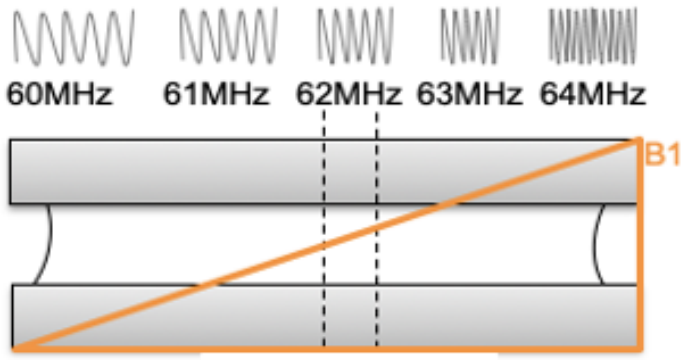


Figure 4: MRI layer selection

Since the development of the MRI, a variety of different so-called sequences have been established, which use different parameters of the resulting signal to generate an image.

### 2.7.1 MRI – image contrast

The weighting (image contrast) of MRI images is determined by T1W (T1-weighted), T2W (T2-weighted), and PDW (Proton Density weighted). Key parameters influencing the weighting are the repetition time (TR = Time of Repetition) and echo time (TE = Time to Echo). Depending on the relaxation stage at which the signal is read, the result is either a T1W, T2W, or PDW image [2].

For T1W-weighted images, tissues with a short T1 time appear hyperintense (bright), whereas tissues with a long T1 time appear hypointense (dark). The T1 time indicates the duration required for hydrogen atoms, post-excitation, to return to longitudinal magnetization. The TR influences the T1 time because it determines how long the hydrogen atoms have to return to their original position. Tissues, such as fat, relax quickly and, upon a new excitation, emit a robust signal, appearing hyperintense. While, tissues like cerebrospinal fluid, with a long T1 time, have not relaxed during a short TR, emit a minimal signal, and appear hypointense on MRI images [2], [50].

In T2W-weighted images, tissues with a short T2 time appear hypointense, while those with a long T2 time appear hyperintense. The echo readout occurs later than in T1W images, which means tissues, such as cerebrospinal fluid with an extended T2 time, still have a substantial signal and appear hyperintense [2], [50].

In Proton Density-weighted images, tissues rich in hydrogen atoms are represented as hyperintense, while those with fewer hydrogen atoms appear hypointense. Only those hydrogen atoms that are in the excited state at the time

of measurement are intended to emit a signal. A short TE and extended TR minimize T1W and T2W influences. PDW-weighted images present a gray-white overall impression, with liquids and fats appearing nearly isointense [2], [50].

# 2.8 Combination of PET and MRI

PET/MRI-scanners are a hybrid imaging technology which combines soft tissue morphological imaging and functional imaging. This integration offers significant advantages in clinical and research settings, allowing simultaneous, multi-parametric imaging [51], [52].

The concept of integrating stand-alone PET with MRI first emerged in the 1990s [63]. By 1996, the introduction of MR-compatible PET detectors made it feasible to conduct PET assessments within strong magnetic fields. This advancement paved the way for preclinical hybrid PET-MR systems, which were designed to facilitate simultaneous PET and MRI scans. Transitioning PET/MRI systems from preclinical to clinical applications posed significant challenges, primarily due to the technical issues involved in merging standalone clinical PET and MRI systems [51], [53]. The development of the clinical PET/MRI system was undeniably influenced by the success of PET-CT. An integrated PET/MRI system offers distinct advantages over PET-CT, particularly in the domain of neuroimaging.

Beyond its superior soft-tissue contrast, MRI offers a diverse range of pulse sequences, enabling non-invasive brain exploration. Given that an integrated PET-MRI system delivers spatially co-registered PET and MR datasets, the structural insights derived from MRI can enhance both the quantitative and qualitative aspects of the PET data. From a research perspective, comprehensive PET-MR protocols, which include PET assessments paired with simultaneous MRI techniques such as T1-MRI, blood oxygenation level dependent-functional MRI (BOLD-fMRI), diffusion weighted (DWI), dynamic contrast enhanced (DCE), and spectroscopy, can be used to understand the body's dynamic processes [51], [52], [2].

### 2.8.1 Technical challenges of hybrid PET/MRI

The integration of PET and MR systems demanded a series of innovative technical advancements, because of compatibility concerns between the two platforms [51]. The interferences between PET and MRI components, in particular, the strong static magnetic field and the rapidly changing gradients of the MRI disrupted the regular operation of the Photomultiplier Tubes (PMTs) and associated PET

circuitry. The homogeneous magnetic field deviated electron pathways, causing a loss in signal gain. Meanwhile, the gradient fields introduced Eddy currents in the PET systems, leading to heat generation and mechanical vibrations. Additionally, Radio Frequency interference from MRI's transmission coil profoundly affected the PET electronics, thereby altering the PET count-rate [51]. On the other hand, PET electronics could introduce inconsistencies in the MRI's primary magnetic field, B0. Given the high sensitivity of MRI receiver coils, designed to pick up delicate Magnetic Resonance signals, interference from similar frequencies, for instance, 120 MHz at 3T, compromised the clarity of MRI outputs [53].

Each individual system typically had an inner bore diameter between 60-80 cm. In order to achieve integration, resizing in one of these systems was unavoidable. By reducing the thickness of the PET detectors, they were seamlessly integrated into the MRI's bore, preserving the necessary Field of View for whole- body imaging.

In response to these challenges, Philips Healthcare introduced the first market-ready PET/MRI system, named the Ingenuity TF [54]. This innovative solution combined a conventional 3T whole-body MRI system with a modified Time-of-Flight (TOF) PET system, separated by a moveable bed mechanism. This spatial avoided interferences between the systems, while traditional PMTs remained shielded. Although, this configuration, enabled spatially synchronized PET and MRI images, they could not ne acquired simultaneously.

One of the main obstacles on the way to a holistic PET/MRI integration was the usage of PMTs. As a solution, solid-state photo detectors (SSPDs) were developed to efficiently identify photon pairs even within strong magnetic fields [55], [51]. The most prominent SSPDs for PET/MRI applications were Avalanche Photodiodes (APD) [66] and Silicon Photomultipliers (SiPM) [56]. Within SSPDs, incident photons genarated electron-hole pairs that are promptly captured by the inherent electric field of the device. Since the path traveled by the charge is minimal, they remain resistant to the powerful magnetic fields produced by the MRI. Siemens set a significant milestone with the release of the integrated PET/MRI system, the Biograph mMR, by transitioning from PMTs to APDs, thus enabling simultaneous PET and MRI data acquisition [57]. The detector unit of this system is located between the gradient and body coils of a 3T whole-body MRI and consits of eight rings, each with 56 detector blocks, where each block contains 8 x 8 LSO crystals connected to a 3 x 3 APD array.

Following the introduction of Siemens' Biograph mMR, GE Healthcare showcased their solution, the SIGNA PET-MR [58]. This version also featured a PET detector ring within a 3T MRI system, leading to a 60 cm internal bore diameter and a 25 cm axial FOV. GE opted for lutetium-based scintillators in tandem with SiPMs for

their PET detectors. By leveraging these detectors, GE incorporated Time-of-Flight PET technology into the SIGNA PET-MR, marking it as the exclusive TOF PET-MRI system with a coincidence timing resolution below 400ps [59], [28].

### 2.8.2 Attenuation correction in PET/MRI

The accuracy of PET images is notably influenced by factors such as attenuation and scatter. In PET-CT, the extraction of PET attenuation components was traditionally achieved by converting the Hounsfield units extracted from the corresponding CT image using a specific bilinear scaling that is sensitive to tube-voltage[28], [29]. However, for systems like the PET/MRI, a challenge emerges. The attenuation components must be derived directly from MR images. This is complex because MR data predominantly showcases the proton density and T1, T2 relaxation attributes of tissues, not the electron densities that determine attenuation. Given this, there has been a common effort to extract accurate attenuation maps from MR images. The precision of the final reconstructed PET image leans heavily on the correctness of this attenuation map [30].

Various methodologies have been introduced for MRI-based attenuation correction, especially when examining the brain. These can be categorized into the following four groups:

- **Atlas-based Approaches:**

  These methods involve aligning a subject's MR image (such as T1, T2, or UTE) to a reference database containing paired MRI-CT or MRI-transmission (TX) AC maps. The procedure typically follows two phases: the atlas MR in the pre-established space is mapped onto the subject's native MR image through affine co-registration techniques. Subsequently, this transformation is extended to the atlas CT-TX image, generating a specific CT-TX image for the subject. However, because these strategies heavily rely on templates from subjects with normal anatomy, their effectiveness diminishes with subjects that display abnormal anatomical morphology [60], [61].

- **Segmentation-based Strategies:**

  These techniques derive attenuation maps directly from MR images, offering stability even when faced with anomalous subject anatomy. The principal of segmentation-based strategies is to segment the MR image into distinctive tissue classifications, for instance, soft tissue, air, and bone, and then assign corresponding attenuation coefficients to each tissue classification. While MR images from specific sequences, like UTE or ZTE,

are effective in capturing bone data, others like Dixon sequences might not sufficiently highlight bone, leading to potential biases [62]. Furthermore, some challenges arise in delineating bone accurately, as these sequences sometimes either overestimate or underestimate bone presence in the skull and neck region. One limitation of this method is its reliance on a fixed attenuation value for specific tissue types, overlooking the potential variations in a tissue's attenuation characteristics, such as with bone[30], [62]. To address this constraint of having discrete attenuation values, a range of strategies that yield continuous attenuation values for bone have been proposed [63], [64]. These approaches leverage sophisticated segmentation techniques and use a derived model between R2* values from UTE images and HU values from CT images to determine bone attenuation values generated to individual patients. As anticipated, attenuation maps with continuous values were superior over those with discrete values [64]. Additionally, these segmentation-oriented MRI AC techniques are not only more user-friendly but are particularly apt for clinical scenarios, especially when patients with irregular cranial shapes due to medical interventions or illnesses are scanned [65], [66], [67].

- **Machine-learning-based Techniques:**

  With the emergence of advanced deep learning algorithms, studies have demonstrated the possibility to produce pseudo CT images from MR images. This procedure generally involves two primary phases: first, the creation of an MR-CT database, and second, a training period focused on the relationship between MR intensity and the corresponding CT Hounsfield unit values. The MR-CT database consists of spatially aligned datasets from various subjects, eliminating the need to align an individual's MR image with the MR-CT database to derive the CT attenuation coefficients. Deep learning methodologies offer an advantage in their robustness, particularly when processing complex signals with noise [68], [69].

- **Reconstruction-based Techniques:**

  Reconstruction-based methodologies extract attenuation correction factors utilizing emission data or by combining emission data with transmission data or using data from scatter coincidences. Initial methods relied on leveraging the consistency conditions inherent to the Radon transform. However, these techniques never became standard in clinical practices. More recent efforts, such as those employing the MLEM algorithm [70],

have shown promise, especially when they incorporate Time-of-Flight (TOF) data to refine the outcomes [71]. The maximum-likelihood expectation maximization (MLAA) algorithm, which was proposed by Nuyts et al., could derive an attenuation sinogram using only emission data [70]. The process required accurate count statistics and was limited by the cross-talk artifacts due to interferences between emission and attenuation data. Introducing Time-Of-Flight (TOF) data and implementing spatial constraints (from sources like MRI) reduced the cross-talk artifacts significantly [71]. Moreover, combining transmission scans with emission scans offers another promising approach for producing an attenuation-corrected PET image. This concept, initiated by Clinthorne et al., aimed to distinctly separate transmission from emission data. Contemporary studies suggest that employing TOF information can successfully achieve separation of emission and transmission data [72].

Commercial PET-MR systems on the market typically offer solutions aligned with either atlas-based or segmentation-based methodologies.

Specifically:

- Siemens Biograph mMR presents three distinct MRI-AC types:
  - two-point Dixon AC that does not consider bone distribution [73], [74]
  - UTE-based AC that does in corporate bone distribution [74]
  - atlas-based AC that supplements the Dixon AC map with bone data using a singular atlas [75]
- GE Signa PET-MR provides two variations of MRI-AC:
  - atlas-based methodology
  - ZTE-based methodology [62]

In a comparative study, Ladefoged et al. [30] analyzed 11 distinct MRI-AC techniques, excluding those based on deep learning, to assess their accuracy in brain MRI-AC applications. The findings revealed that the performance of all 11 MRI-AC methods remained within the generally accepted bounds, deviating by no more than ± 5% from CT-AC benchmarks. It's worth noting that the precision of MRI-AC concerning image-derived input functions and the standard database remains under-explored. However, a later publication resulting from this research explores deeper, evaluating a modern MRI-AC in the context of IDIF and a normative database [30].

## 2.9 Dynamic 18F-FET-PET examination in glioma

As the prognosis of different types of gliomas and their severity varies patients benefit from an early and reliable diagnosis. Histological examinations are associated with surgical intervention and are correspondingly risky. Therefore, the dynamic 18F-FET-PET has been established as an important diagnostic tool in the management of gliomas.

In order to study metabolic processes of the body it is helpful to analyze static information such as the result of an accumulation of a substance and dynamic information such as the transport of a tracer through the body.

The current guidelines advocate the analysis of the tumor's time-activity curve (TAC) relative to healthy brain tissue. This involves graphically representing the curve progression and making a visual assessment. Multiple studies have shown that a TAC exhibiting a plateau formation or a rapid decline following an initial increase indicates a more aggressive tumor [76], [77].

Building on this, numerous studies have aimed to enhance the prognostic accuracy. For instance, researchers have correlated the TAC shape with glioma progression time [88], various glioma mutations [8], [78] and particularly aggressive regions within the tumor. Other studies have delved into questions concerning therapy success, recurrences [79], [77], and differentiation from metastases [80]. Most of these issues were further studied using static 18F-FET- PET examinations [5], [77], [79].

Several new analytical approaches have also been published. Under the umbrella term "radiomics," some studies have conducted textural analyses of gliomas [81], [93] established links to specific MRI sequences [82], [83], and employed artificial intelligence algorithms [84], [85].

Pharmacokinetic modeling for 18F-FET-PET has also been explored in some studies, primarily focusing on determining the optimal model for the entire tumor. Publications by Bolcaen et al. 2016 [86] and Richard et al. 2017 [87] investigated pharmacokinetic modeling of 18F-FET based on glioma formations in rats. In both studies, two-compartment models emerged as the most effective. Koopman et al.'s 2018 study, involving seven participants, identified the 2T4k model as the ideal one for the tumor, with a reversible model predominant in healthy brain tissue. This study used a directly measured arterial input function [88].

Röhrich et al., in 2018, published a study with 44 participants where pharmacokinetic modeling aided in distinguishing between WHO Grade 4 and Grades 2/3. A 2T4k model was employed, and the input function was sourced from PET scans near the carotid arteries. Significant differences were observed in the relative k1 values between glioblastomas and low-grade gliomas [8].

Apart from the initially introduced TAC analysis, no other analysis method has made its way into clinical practice recommendations. This can be attributed to consistently weak diagnostic accuracy or small study sizes, despite the presence of significant results as present in the studies above.

The full potential of kinetic modeling has yet to be achieved. Embarking on such studies presents considerable challenges. Not only is it difficult to obtain dynamic raw data, but the necessity of high-cost analytical software presents another difficult obstacle.

Research is evolving towards a streamlined and universally applicable implementation. The system should work independently and pave the way for machine-based analyses. By employing kinetic modeling for each individual voxel, a more precise representation of inconsistencies both within and surrounding a glioma can be achieved. This advancement marks a significant step towards non-invasive diagnostics.

In Poglitsch's dissertation titled, “Kinetische Modellierung bei dynamischen 18F-FET-PET Untersuchungen von Gliomen” the main goal was to design a program that allows for the automatic kinetic modeling of an 18F-FET-PET examination of the brain. In the pilot study a software was developed to enable clinicians and researchers to perform streamlined pharmacokinetic modeling. The program generates parametric maps detailing pharmacokinetic variables vB, k1, k2, k3, and k4, an 18F-FET-PET/MRI analysis. Subsequent maps can pinpoint inequalities between gliomas and normal brain tissue [7].

Validated with a sample of eight patients, the produced parametric maps were set against gliomas' histologic diagnosis and conventional 18F-FET-PET/MRI evaluations. As a result, the optimal pharmacokinetic model was determined as the two-tissue reversible plasma (2T4k) model. It is important to note that, while significant variances between gliomas and healthy brain tissue were evident with this model, the study's limited sample size made differentiation based on histological diagnosis inconclusive [7].

The pilot study underscores the potential of pharmacokinetic modeling in 18F-FET-PET/MRI glioma imaging and offers an accessible software tool for future researchers.

## 2.10 Hypothesis of the thesis

The main goal of this thesis is to integrate a state-of-the-art partial volume correction technique to advance quantitative accuracy in kinetic modeling, specifically for image-derived input-function (IDIF) extraction. Hence, the time-sensitive activity concentration in the tissue adjacent to the carotid arteries will be evaluated, leading to the development of a respective spill-in and -out correction that is both time and tissue dependent. The result of this thesis is a quantitative accurate IDIF for kinetic modeling.

In addition to the main goal, this thesis will implement a robust motion correction and thereby tackle the challenges posed by patient motion during a 40-minute PET scan. The objective is to reduce the impact of patient motion in between the frames of the acquired PET data, ensuring that the data used in kinetic modeling remains as accurate as possible. By addressing the issue of motion artifacts, the precision and reliability of this quantitative analysis will be enhanced.

**Main Hypothesis:**

1. The developed Image-Derived Input Function can provide quantitatively accurate representations of tracer concentrations over time for kinetic modeling, eliminating the need for invasive arterial blood sampling.

# 3 Material and Method

Between 2015 and 2020, the University Department of Radiology and Nuclear Medicine at the Medical University of Vienna, situated within the General Hospital of the City of Vienna, carried out a total of 334 dynamic 18F-FET-PET examinations for suspected brain tumors. Of these, 176 examinations were carried out on the Biograph TPTV 64 PET-CT scanner, while the remaining 158 examinations were conducted using the Biograph mMR PET/MRI device, both provided by Siemens Healthcare GmbH, Erlangen, Germany. Out of the 334 examinations conducted only 8 were used for the final study group. The primary criteria for exclusion is explained in the following chapter. The retrospective data collection and exploratory data evaluation was approved by the ethics committee of the Medical University of Vienna, under code EK 1075/2020.

## 3.1 Patient data

The study group comprises datasets from 3 female patients and 4 male patients, ranging in age from 22 to 63 years, diagnosed with brain tumors such as astrocytoma, oligodendroglioma and glioblastoma, as listed in table 1.

| Number | Gender | Age | Diagnosis |
|---|---|---|---|
| **007** | Female | 22 | Astrocytoma |
| **009** | Female | 47 | Astrocytoma |
| **035** | Male | 63 | Astrocytoma |
| **052** | Male | 40 | Oligodendroglioma |
| **069** | Female | 41 | Glioblastoma |
| **074** | Male | 49 | Glioblastoma |
| **090** | Male | 29 | Glioblastoma |

Table 1: characteristics of the study group with assignment number, age at examination, sex and diagnosis (Poglitsch)

## 3.2 Exclusion criteria

To ensure a consistent study group, Poglitsch excluded certain examinations. Examinations conducted on the PET-CT were excluded due to the device's inability to save raw examination data, which is crucial for refined reconstructions needed in kinetic modeling. Out of the remaining 158 PET/MRI examinations, 13 datasets were excluded since the subjects were under 18 years old on the day of imaging.

The remaining 145 examinations were roughly categorized based on preliminary diagnoses, resulting in 45 suspected initial brain tumor diagnoses, 82 recurrences, and 17 metastases from other tumors.

To avoid pre-treatments, only the 45 examinations with suspected initial diagnoses were considered. Out of these, 17 displayed no significant changes in 18F-FET uptake in the tumor. 14 did not have a histological examination, with five showing notable FET retention. From the remaining 23 examinations, 15 datasets were either incomplete or untraceable. In the final selection, datasets from 8 patients were considered. However, for the purpose of this research, only 7 of these datasets were included in the study group. One patient´s dataset was excluded due to a late start of the examination, which resulted in missing the initial phase of tracer uptake a crucial component for accurate Time-Activity Curve analysis.

## 3.3 PET MRI protocol

Examinations were performed using a Biograph mMR PET/MRI system from Siemens Healthcare GmbH, Erlangen, Germany. The scanner integrates the PET detector within the MRI setup, specifically between the gradient coils and the radiofrequency excitation coils. It consists out of 8 rings with 56 detector blocks, each block contains 8x8 LSO crystals (4x4x20 mm), coupled to a 3x3 grid of water-cooled APDs. This configuration results in a total of 4032 channels and a voxel dimension of 172x172x127 with a voxel size of 2x2x2 mm^3 [7].

The PET scanning protocol is 40-minute long, initiated by the intravenous administration of approximately 2.8 MBq of 18F-FET per kg of body weight. For this study, the acquired data was reconstructed into 31 sequential time windows (12x5s + 4x15s + 8x1min + 5x4min + 2x5min) using a DIXON-based attenuation correction [7].

The PET/MRI examination was scanned simultaneously and consisted out of various sequences. For this study, the T1 sequences after the administration of contrast agent were used.

# 3.4 Data processing

### 3.4.1 Coding language

In Poglitsch dissertation, he used the Python programming language. His choice was influenced by Python being open-source and supported by a big community. Regularly updated and refined, Python offers a number of freely accessible libraries. Despite being a high-level language, Python offers efficient performance and includes numerous libraries tailored for image processing. A minor disadvantage is that the documentation of some libraries is not accurate. Yet, the flexibility of Python, made it the preferred choice. This rationale informed the decision to use Python for implementing the quantitative accurate IDIF. Sundar created an image-derived input function for his dissertation using MATLAB [7], [42], and the structure of his function served as a reference for generating a similar function in Python. The next chapter describes the used libraries and developed function that were needed to generate a quantitative accurate IDIF.

### 3.4.2 Libraries

The Program was developed using standard Python libraires, each serving a specific purpose to enhance its functionality. These libraries include standard Python libraries, well-established open-source libraries, as well as specialized ones tailored for scientific publications and software frameworks.

- os: This library played a crucial role in accessing specific file locations, ensuring seamless file operations within the program.
- gc: For the program the 'gc' library was used, which allowed for the release of unused memory space, optimizing performance.
- argparse: Command-line interaction was facilitated by the 'argparse' library, which enabled the creation of user-friendly command-line inputs.
- time: To incorporate time-related functionalities, the program accessed the 'time' library, allowing it to interact with and utilize the current time as needed.
- multiprocessing: The program used the power of process-based parallel computing through the 'multiprocessing' library, enabling efficient multitasking.
- numpy: For effective manipulation of matrices and arrays, the 'numpy' library was employed, simplifying complex numerical operations.
- scipy: Extensive scientific programming capabilities were realized with the inclusion of the 'scipy' library, offering a wide range of scientific and technical computing functions.

- matplotlib: A key component for creating graphical representations, 'matplotlib' enabled the generation of static, interactive, and animated visualizations within the program.
- SimpleITK: As the Python adaptation of the 'Insight Segmentation and Registration Toolkit' (ITK), 'SimpleITK' played a pivotal role in advanced image processing tasks within the program.
- lmfit: For addressing non-linear optimization problems, 'lmfit' was incorporated as a versatile Python software solution.
- ray: Facilitating efficient distribution of large, parallelizable tasks across multiple processors, 'ray' served as a valuable addition to the program's capabilities.
- nibabel: Handling medical imaging data was made seamless with the nibabel: library, specializing in reading, and writing nifti files, a common format in the field.

### 3.4.3 Program

For this thesis two advanced techniques were adapted a motion correction and a partial volume correction which include spill in and spill out corrections.

The objective of motion correction in PET imaging is to account for any patient movement during the scan, ensuring that motion between frames is corrected. This guarantees that the Regions of Interest (ROIs) align accurately throughout the entire PET dataset. The integrated motion correction processes each frame of the PET scan comparing it to a reference frame.

Each frame is aligned to match the reference frame. The program calculates how much each frame needs to be shifted (translated) and rotated to match the reference frame. This calculation involves determining the best combination of movements (up/down, left/right, forward/backward) and rotations (around the x, y, and z axes) that make the current frame align closely with the reference frame.

Once all frames are aligned with the reference frame, motion artifacts in between frames are minimized.

The purpose of the PVC is to correct for the spreading (spillover) of the signal from small structures, like the carotid arteries in the brain. This spreading can make these structures look larger than they are and can mix their signal with surrounding tissue.

The PVC code addresses two main issues - spill-out (where the signal from a structure seems to leak into surrounding areas) and spill-in (where the signal from surrounding areas seems to leak into the structure).

It applies mathematical filters to estimate how much signal has spilled in or out and thereby adjusts the signal for the PET data. During each iteration, the PVC checks how much the corrected data has changed from the previous data. Once the changes become small enough, it stops because further corrections won't significantly improve the image. The outcome of PVC is a more accurate representation of signal in the scanned region.

The following two chapters describe in detail how the motion correction and partial volume correction work.

### 3.4.4 Motion Correction code

The goal of implementing a motion correction in this thesis was to minimize the impact of patient movement during a 40 min. long brain FET PET/MRI scan. Brain imaging, especially in a neurological or oncological context, often requires high precision due to the small size and close proximity to the structure of interest.

This thesis specifically addresses head movements, opting for rigid registration as the method of choice. The rigid registration can compensate for frequent head movements such as slight tilts or rotations that often occur during longer scanning sessions. The choice of rigid registration was also influenced by its computational efficiency and speed, which are well compatible with the time-critical requirements of clinical workflows.

The motion correction is set up as a “software pipeline” which makes it easy to update and use. The individual components of this program part are shown in Figure 5 and are described in detail in the next section.

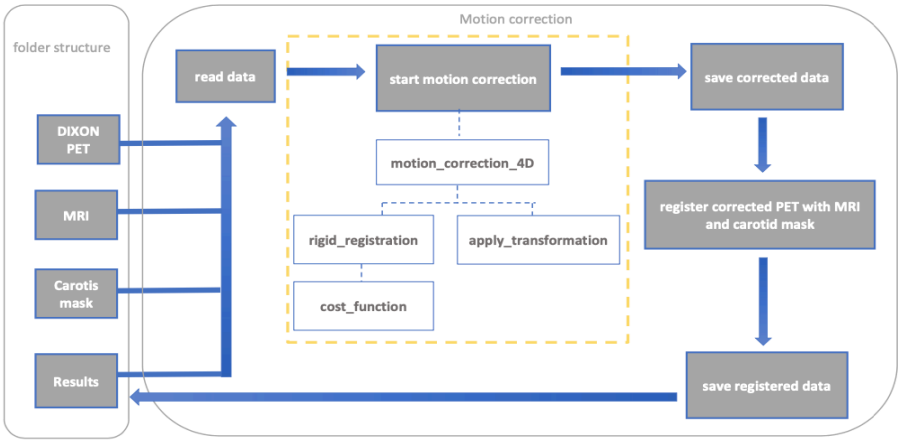


Figure 5: Motion correction pipeline

The motion correction pipeline for this thesis is designed to address movements that occurred between each frame during the scan. It consists out of three main functions. The primary function, “rigid_registration(fixed, moving)”, aligns a “moving” image to a “fixed” image using rigid body transformation, which involves translation and rotation. Within this function, a nested “cost_function” calculates the cost for a given set of transformation parameters. This calculation is performed using an affine transformation that applies translations (dx, dy, dz) and rotations (theta_x, theta_y, theta_z) to the moving image. The cost is determined as the negative cross-correlation between the fixed and the transformed moving image, with the objective being to find parameters that minimize this cost, thereby optimizing the alignment between the two images. To achieve this optimization, Powell's method (algorithm for optimizing mathematical functions) [89] is employed to find the transformation parameters that minimize the cost, striking a balance between computational efficiency and precision in alignment.

The subsequent function in the motion correction pipeline is titled “apply_transformation(image, params)”. This function is instrumental in implementing the transformation parameters previously computed. It initiates by constructing individual rotation matrices corresponding to the rotation parameters (theta_x, theta_y, theta_z) for each of the three axes. These matrices are then combined to form a comprehensive rotation matrix. Next, the affine transformation process is engaged, using the rotation matrix in combination with the translation parameters (dx, dy, dz). This integrated approach enables the precise alignment of frames, ensuring the accuracy and reliability of the motion correction process.

The central component of the motion correction pipeline is the "motion_correction_4d(data_4d, affine, output_path)" function. It begins by determining the total number of frames within the 4D PET data. In the next step the reference frame is selected. In this study, the reference frame for alignment is a frame from the first few minutes of the scan where the whole brain is adequately visible. This approach minimizes the risk of misalignment due to patient motion at the very beginning of the scan and it avoids the initial period immediately after tracer injection where registration might fail due to lack of signal in the beginning. Therefor the frames leading up to the reference frame were not registered to it. Further, the selection of the reference frame is based on visual inspection of the PET data to identify the first frame where the entire brain is visible. For all PET data sets in this thesis the reference frame was chosen individually. This is crucial for effective image registration and ensures a comprehensive coverage of the brain.

Upon establishing the reference frame, the function initializes a new data array to store the motion-corrected frames. This array mirrors the dimensions of the input data, ensuring consistency in data handling. The core of the function lies in the iterative processing of each frame within the PET dataset. For every frame, the "rigid_registration" function is called to calculate the necessary rigid body transformation, encompassing both translation and rotation, to align the current frame with the reference frame effectively.

The computed transformation parameters are then applied to the current frame through the "apply_transformation" function. This crucial step adjusts each frame to align precisely with the reference frame, thereby compensating for any patient motion during the scan. The result is a set of motion-corrected frames which are essential for reliable PET analysis. By correcting for motion between different frames, this process ensures that the carotid mask aligns consistently across the entire scan, effectively minimizing discrepancies caused by patient movement and enhancing the precision of the analysis.

Following the motion correction, it is essential to register the motion corrected PET data to the MRI scan. This registration ensures that anatomical structures are accurately aligned to the PET data.

The following image 6 shows how the alignment of the MRI, PET and carotid mask was validated.

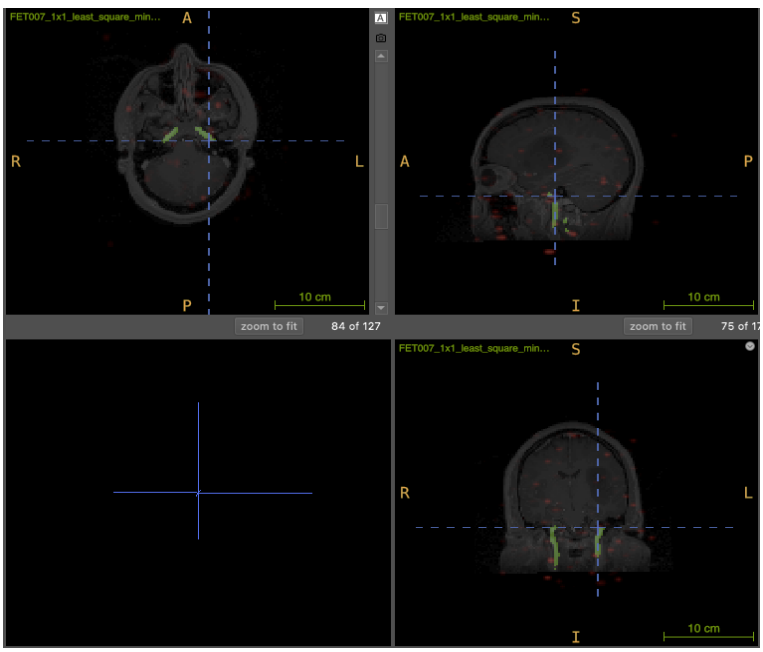


Figure 6: alignment of MRI, PET and carotid mask

### 3.4.5 Input function code

For an accurate extraction of the IDIF a prior PVC is required to ensure precision in tracer concentration measurements. The goal of implementing a partial volume correction is to reduce the inaccuracies caused by the limited spatial resolution of the PET/MRI scanner which lead to the partial volume effect. This effect causes the signal of the tracer to appear “smeared”, with activity spilling from the region of interest (ROI) into adjacent areas and vice versa. Specifically, spill-in occurs when the signal from the trace of the surrounding tissues leaks into the ROI, which wrongly increases the tracer signal inside the ROI. Spill-out occurs when the signal of the tracer within the ROI leaks into adjacent areas, resulting in a lower tracer signal within the target area. Implementing a PVC significantly improves the accuracy and reliability of quantitative image analysis.

Sundar et al. established a methodology for spillover correction specifically tailored to the tracer FDG, aimed to achieve a quantitative IDIF. From this approach, the spillover correction for this thesis was adapted and refined to suit the characteristics of the FET tracer.

The partial volume correction is set up as a “software pipeline”. The individual components of this program part are shown in Figure 7 and are described in detail in the next section.

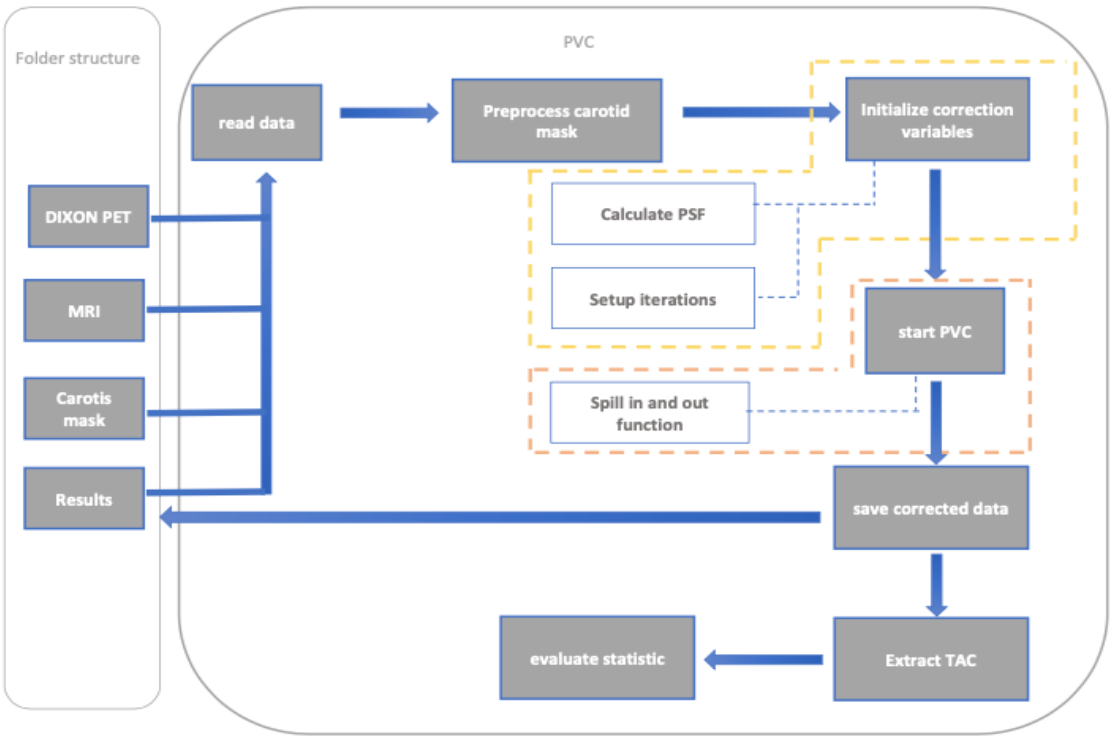


Figure 7: Partial volume correction pipeline

The partial volume correction pipeline consists out of seven functions. Each of these functions plays a specific role in accurately processing and analyzing the data. In the following section first each function will be explained and afterwards how the whole program works.

The “calculate_psfSigma” function is a fundamental component in the partial volume correction process, specifically designed to calculate the standard deviation (σ), or “psfSigma”, for a Gaussian Point Spread Function (PSF). This calculation is essential for accurately modeling the spread of the tracer in the PET imaging process.

The process begins with the extraction of voxel dimensions from the input image, identified as “xDim”, “yDim”, and “zDim”, using the “GetSpacing()” method. These dimensions represent the physical size of each voxel in the PET dataset across the x, y, and z axes. This information is crucial for understanding the spatial resolution of the PET image.

To accommodate variations in the Full Width at Half Maximum (FWHM) input, the function assesses whether “psfFWHM” is provided as a single value (scalar) or as multiple values (vector). In the case of a scalar, isotropic filtering is assumed, indicating uniform blurring across all dimensions. The scalar is then replicated across all three dimensions to create a uniform array. However, if “psfFWHM” is already a vector, it is directly converted into a numpy array for subsequent processing.

Finally, the function calculates “psfSigma” from the “psfFWHM” values. This is achieved using the formula “psfSigma = psfFWHM / np.sqrt(8 * np.log(2))”, which translates the FWHM into the standard deviation of the Gaussian function.

The function concludes by returning the calculated “psfSigma”, which is now primed for use in Gaussian filtering operations within the partial volume correction process. This value of “psfSigma” plays an important role in the accurate simulation of the tracer's signal spread.

“apply_psf_to_mask” function models the PSF by applying a Gaussian filter to the carotid mask. It simulates how the PSF would cause the signal of the radioactive trace to spread out of the ROI and into the neighboring voxels. The output of this function is the “spill_out_zone”, which is a data set that shows potential spill-out areas, reflecting how the signal from withing the carotid mask blurs into surrounding tissue. This zone serves as the basis for adjusting the PET data to compensate for spill-out effect.

Another mask is created by using binary dilation to identify the immediate neighboring voxels around the carotid mask. A neighbor kernel which is a 6x6x6 cube around the ROI is created. The new mask specifically excludes the areas within the carotid mask, thereby focusing on the neighboring voxels where spill-in typically occurs. This approach ensures that corrections are accurately targeted to the areas most affected by spill-in artifacts.

The “create_background_mantel” function uses the neighboring kernel mask to create the background mantel. It addresses this by dilating the mask 10 mm) to capture a broader area that might be affected by spill-in, thus creating a background mantel.

After creating the background mantel, which includes potential spill-in regions, the function “segment_background_mantel” refines the area to focus corrections more precisely. It applies Otsu´s thresholding method to the “background_mantel”. Regions with significant signal from tracer activity above a calculated threshold are segmented out and provide a targeted zone for applying spill-in corrections. This ensures that corrections are not uniformly applied across the entire mantel, which might include regions without significant tracer spill-in, thereby avoiding over-correcting areas.

The main and most important function is the “spill_correction_volume”, it applies iterative corrections to address spill-out and spill-in effects in PET data. It uses a multi-step approach within a loop to refine the PET data iteratively, ensuring each step contributes toward an accurate representation of the tracer distribution.

It starts by duplicating the original PET data to avoid altering the original dataset. In the next step the function enters an iterative loop, designed to refine the correction process up to a maximum of 10 iterations (“numiters”), or until the changes between iterations fall below a certain threshold (“epsilon”). After each iteration, the function compares the newly corrected PET data (“corrected_pet”) with the data from the previous iteration (“PET_prev”). If the relative change is less than “epsilon” it indicates that further iterations are unlikely to significantly refine the data and the loop terminates.

The last function is the “extract_tac” function. It plays an important role in the processing of PET data, specifically designed to extract the Time-Activity Curve (TAC) from a dynamic PET dataset. The primary purpose of this function is to calculate the average tracer concentration for each time point within the ROI, in this case, the carotid region. This is achieved by focusing on the area delineated by the “carotid_mask”, which is a binary mask where voxels within the carotid ROI are marked as true (1) and others as false (0).

The function initiates its operation by identifying the indices within the PET dataset that correspond to the carotid region, as indicated by the “carotid_mask”.

For the 4D PET data, which includes both spatial and temporal dimensions, the function first establishes the number of time frames present in the dataset. It then initializes a zero-filled array “tac”. Next the function iterates over each time frame, calculating the mean tracer concentration within the carotid region for that specific time frame. This calculated mean value is stored in the “tac”. The function concludes by returning the tac array which encapsulates the average tracer activity within the carotid region across all time frames.

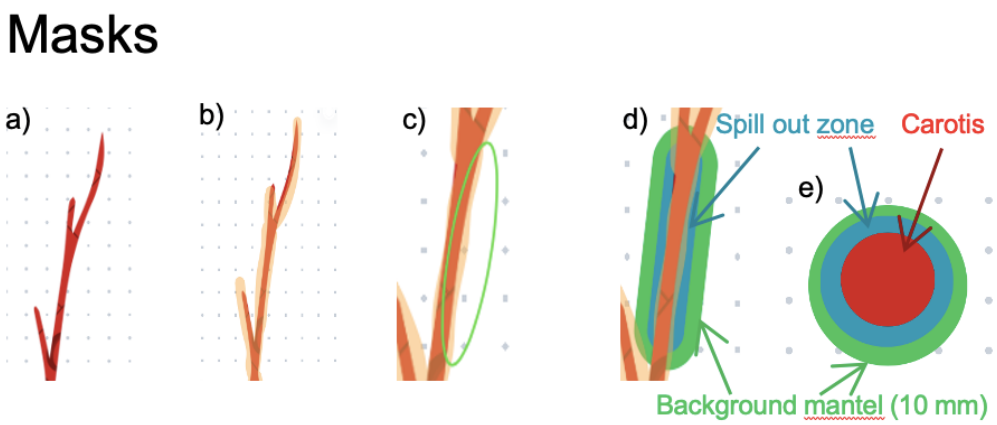


Figure 8: masks: a) shows a part of the carotis, b) shows the carotis after tracer injection, c) shows the spill-out area, d) shows the spill-out zone which is depended of the PSF (FWHM 6mm) and the background mantel of 10 mm around the spill-out zone.

The whole program works as follows:

The program starts by loading the PET data and a predefined carotid mask (ROI). The carotid mask is used to simulate how the signal of the tracer might have spread outside the ROI due to the PET scanner´s partial volume effects.

**Spill-Out Zone:** First the carotid mask is used to create a spill out zone, indicating potential areas where the signal appears to have spilled out of the ROI.

**Neighboring kernel mask:** To address the spill-in correction a neighboring kernel mask is created; this mask identifies the immediate neighbors of the ROI. This mask is further processed by dilating it to create a background mantel to include a broader area around the ROI. The background mantel helps to ensure that spill-in corrections are not too narrowly focused.

**Mantel segmentation:** In the next step the background mantel is segmented by Otsu´s method. It isolates areas that have a signal above a certain threshold to ensures that corrections are not uniformly applied across the entire mantel.

**Iterative correction:** During each iteration of the correction process a gaussian filter models the spread of the tracer signal to estimate both spill-out and spill-in effects. Corrections are iteratively applied based on the segmented mantel for spill-in and the spill_out_zone mask for spill-out. This process continues until the changes between iterations are minimal.

**End of the pipeline:** In the last steps the estimated spill-out is added to the PET data to compensate for underestimation, while the estimated spill-in effect is subtracted to correct for overestimation. This approach ensures that both spill-out and spill-in effects are corrected.

### 3.4.6 Statistical methods

Medical imaging plays a crucial role in healthcare, providing clinicians and researchers with insights into the physiological processes within the human body. In PET/MRI imaging, challenges like partial volume effects (PVE) and motion artifacts can significantly affect image quality and quantitative accuracy.

To address these challenges, this master's thesis focuses on the implementation and adaption of a robust motion correction technique, alongside spill-in and spill-out corrections, to obtain an accurate quantitative IDIF. The efficacy of these corrections was assessed using two parameters (AUC and Peak Activity) and the paired t-test for statistical evaluations.

- Area Under Curve (AUC):
  AUC provides a comprehensive measure of the tracer's concentration over time within the region of interest. It's particularly useful for comparing the overall tracer uptake before and after applying corrections.
- Peak Activity:
  This metric indicates the maximum tracer concentration observed in the region of interest. It's crucial for assessing the effectiveness of correction techniques.
- Paired t-test:
  Since the paired t-test is specifically designed to compare two related groups it was used for this master´s thesis. Therefore, two sets of data are given – IDIF before and after correction. By comparing pre- and post-correction images within the same patients it can be determine whether the corrections have statistically significant changes.

The process of extracting the values, statistics and generating Time-Activity Curve graphs from PET data involved several steps, using the capabilities of Python's analytical and visualization libraries. Graphical comparisons of the uncorrected and corrected TACs for the same patient data were crafted using “matplotlib.pyplot”. These plots display time in seconds on the x-axis against the average tracer concentration on the y-axis, representing the differences between the two datasets.

Key quantitative insights were obtained by calculating the Peak Activity of each dataset, identified as the maximum value within the TAC (np.max). This approach provided a clear understanding of the highest tracer concentrations observed in both the uncorrected and corrected datasets.

Furthermore, the AUC was quantified using the trapezoidal rule (np.trapz), offering a comprehensive measure of the total tracer concentration over time.

To statistically evaluate the differences between the uncorrected and corrected TAC data, a paired t-test (ttest_rel) was performed. The resulting t-statistic and p-value were calculated and reported, providing a robust statistical foundation to assess the significance of the changes observed post-correction. Further the median and Interquartile Range (IQR) for the Area Under the Curve (AUC) values were calculated.

By following this structured approach, the thesis comprehensively analyzes the PET data, providing both a visual and statistical comparison of the uncorrected and corrected datasets. This methodological process ensures that the conclusions drawn are supported by both graphical trends and statistical analysis.

Since a ground truth, such as arterial blood sampling, is missing the effectiveness and accuracy of the PVC implemented in this thesis were validate through a comparative analysis with existing literature. This validation involved comparing the ratios of Area Under the Curve and peak activity concentrations with corresponding values found in literature. This comparative approach helps to ensure that the PVC methods applied are consistent with established results.

# 4 Results

The main result of this thesis was the implementation of a motion correction and quantitative accurate IDIF for automatic kinetic modeling of 18F-FET-PET/MRI brain scans to enable improved non-invasive diagnosis for glioma.

To evaluate the effectiveness of the motion corrected, a qualitative assessment was performed through visual inspection of the corrected PET data. The uncorrected PET data was visually compared against the corrected PET data. This comparison revealed that minor head tilts, initially present in the scans, were effectively corrected through the motion correction. Overall, the PET data showed minimal signs of patient movement, indicating a high level of stability throughout the scanning sessions.

Following the motion correction, the partial volume correction was implemented to address the problem of tissue spillover effects, which are common in PET imaging. These effects occur due to the limited spatial resolution of the scanner, which can blur the signal of the tracer. The generated PVC adjusts the signal of the PET data representing an accurate signal of the tracer concentration. By applying PVC the signal within small structures such as the carotid artery was higher compared to the signal before applying PVC.

### 4.1.1 Data analysis

In this thesis, each dataset underwent motion correction and partial volume correction, from which the Image-Derived Input Functions (IDIFs) were derived. To show the differences between the uncorrected and corrected data, the IDIFs were graphically represented against time, and key values such as the Area Under the Curve, Peak Activity, and a statistical paired t-tests were analyzed.

To validate the effectiveness of the correction methods the corrected IDIF was first compared with the uncorrected IDIF. This comparison helps illustrate the quantitative impact of the PVC method.

In the following section first the graphs, AUC and peak activity for each patient will be presented and afterwards the comparison with literature.

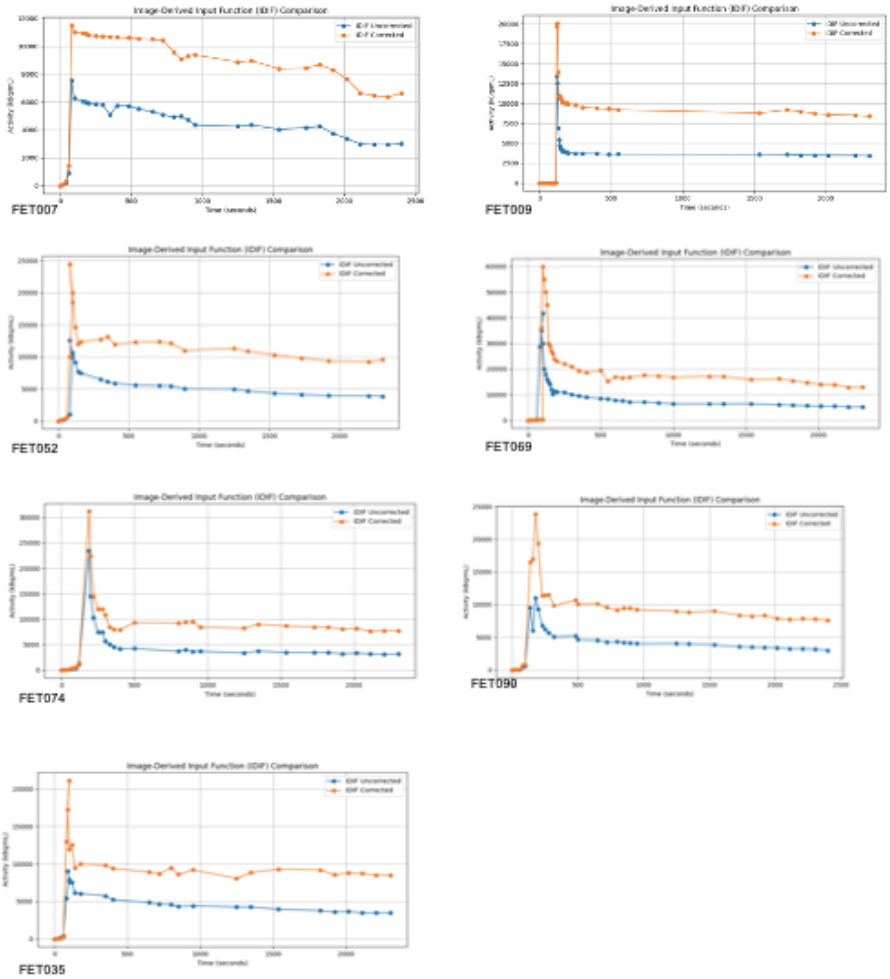


Figure 9: TAC curves

The graphs above present a comparison of the Time-Activity Curves (TAC) for Uncorrected and Corrected PET data over a series of time points for each dataset used in this thesis. The y-axis shows the detected activity in kBq/ml and the x-axis shows the time in seconds. A statistical analysis of each dataset revealed significant differences between the uncorrected and corrected Time-Activity Curves. In the initial phase each graph shows that the uncorrected and corrected curves show minimal activity, indicating low tracer uptake in the initial phase. A significant rise in tracer concentration is observed in all curves after the first minute. The corrected data shows a much higher increase compared to the uncorrected data.

The AUC values were compared between the uncorrected and corrected datasets to evaluate the impact of partial volume correction (PVC). The results show a median percentage increase of approximately 90-110% in AUC values following

correction. To account for the high variability in AUC values and reduce the impact of outliers, a log transformation was applied. The interquartile range (IQR) of the log-transformed AUC values was 1,60.

A paired t-test on the log-transformed AUC values was conducted to determine if there was a statistically significant difference in the values between the uncorrected and corrected data. The results revealed a significant difference between the datasets ($p = 0.0238$). The peak activity was assessed too and showed an increase in all datasets after correction, indicating that the correction method consistently enhances the measured peak activity. The percentage increase in peak activity varies significantly among subjects, ranging from 32.59% (FET074) to 134.85% (FET035). This suggests that the correction method has different effects on different subjects, possibly due to individual differences or varying conditions during measurements. The median increase is 52.69%.

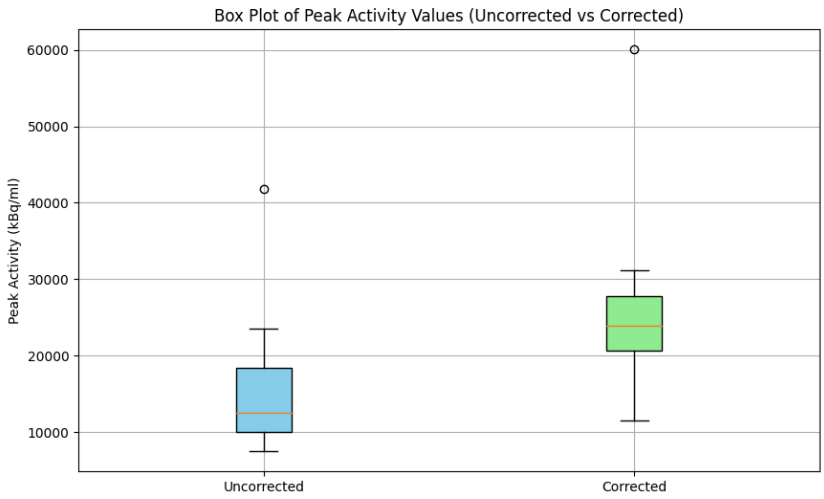


Figure 10: Box Plot peak activity

The box Plot in figure 10 shows the peak activity values. The median peak activity value (represented by the line inside the box) for the corrected data is significantly higher than that of the uncorrected data. This indicates that, on average, the correction process increases the peak activity values.

The interquartile range (IQR), represented by the height of the box, is larger for the corrected data compared to the uncorrected data. This suggests that there is more variability in the corrected peak activity values.

The whiskers, which represent the range of the data excluding outliers, are also longer for the corrected data, indicating a wider range of peak activity values after correction. There are notable outliers in both the uncorrected and corrected data. Specifically, there is one high outlier in each group, indicating extreme peak activity values that deviate significantly from the rest of the data.

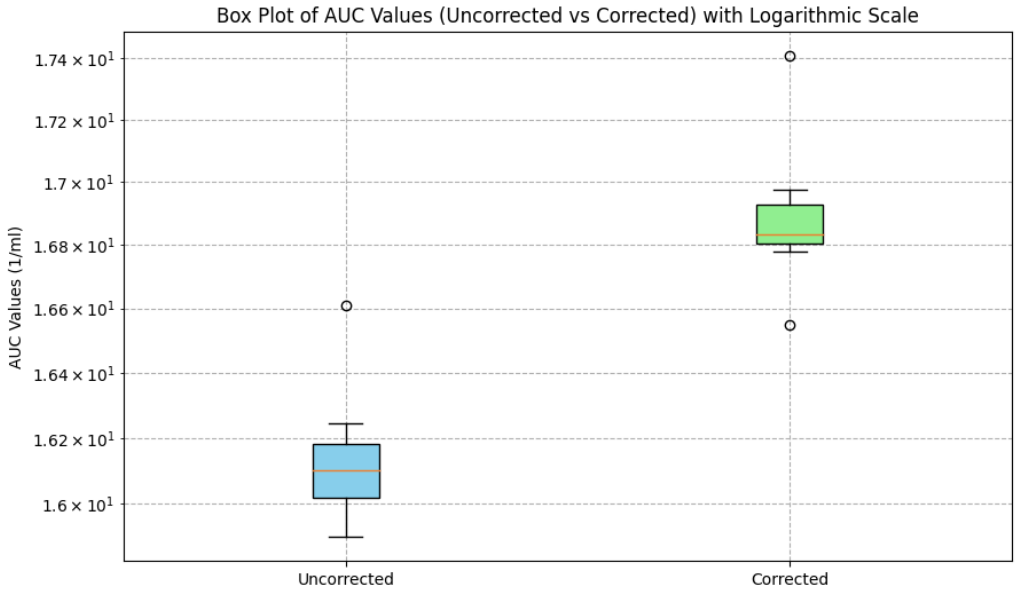


Figure 11: Box Plot log AUC

The box plot shows that the log-transformed AUC values are generally higher after correction. This graph shows that the partial volume correction (PVC) has a significant impact on AUC values and therefore on the IDIF.

The height of each box represents the interquartile range (IQR), which is the range between the 25th and 75th percentiles. The IQR for the corrected AUC values is larger than the uncorrected values, indicating more variability in the corrected data.

The lines extending from the top and bottom of each box show the range of the data, excluding outliers. The correction appears effective in increasing AUC values, potentially enhancing the sensitivity or accuracy of the measurements.

The findings were compared to those reported in literature. Previous studies by Sundar et al. [42], [90]and Sari et al. [90] demonstrated significant improvements in IDIF accuracy and AUC measurements following PVC.

In Sundar´s. research paper [42]. the authors developed a method to non-invasively estimate the arterial input function (AIF) using an image-derived input

function from integrated PET/MRI data. Their approach was validated against the invasively measured AIF, assessing discrepancies in the area-under-the-curve (AUC) measurements between the AIF and IDIF, which demonstrated a high degree of accuracy and consistency, with test–retest variability and absolute percentage differences between cerebral metabolic rates of glucose (CMRGlc) measured via AIF and IDIF [42].

Sundar et al. [42]. reported median absolute differences within ±5% when comparing the IDIF after PVC to the AIF, demonstrating the accuracy of PVC in their study. The increase in AUC values before and after corrections were compared with the results reported by Sundar et al. They observed an 80% increase in AUC values following partial volume corrections. In this thesis, the AUC values increased by approximately 90-110%% after applying PVC. This shows that the findings increased like in Sundar et al. paper. Although direct numerical comparisons are challenging due to differing methodologies, the overall trends highlight the efficacy of PVC.

Sari´s research paper [90] addresses a non-invasive alternative to AIF, it introduces a practical method for extracting an image-derived input function (IDIF) by segmenting the carotid arteries from MR images, thus avoiding the challenges associated with blood sampling and overcoming partial volume effects. A simulation study confirmed the efficacy of the proposed partial volume correction (PVC) technique, with results showing recovery of at least 92% of the true intensity post-correction [90].

Sari et al. [90] reported a significant increase in AUC values post-PVC, with a peak increase of 95% on average. This improvement is consistent with the observed peak increase of 90-110% in this thesis.

# 5 Discussion

The primary objective of this thesis was to refine a pre-existing program designed for pharmacokinetic modeling of 18F-FET-PET data. This refinement involved integrating motion correction to account for patient movement and enhancing the accuracy of IDIF through partial volume correction, which includes adjustments for both spill-in and spill-out effects.

The main result of this work is the implementation of the motion correction and PVC for automatic kinetic modeling of 18F-FET-PET/MRI brain scans to enable improved non-invasive diagnosis of gliomas. The source code of the two pipelines can be found in Appendix 1.

**Motion Correction**

The accuracy of 18F-FET-PET/MRI brain scans can be significantly compromised by patient movement during the scanning process. Even minor head movements, such as tilts or rotations, can introduce substantial artifacts that affect the reliability of the PET data. This thesis implemented a motion correction technique to correct motion in-between frames.

For this thesis a rigid registration method was chosen to correct head movements during scanning. This method aligns images based on translations and rotations, ensuring that the region of interest remains correctly positioned across all frames. The choice of rigid registration was influenced by its computational efficiency and speed, making it well-suited for clinical environments where quick processing is essential [46], [47], [91].

To evaluate the effectiveness of the motion correction, a qualitative assessment was performed through visual inspection of the corrected PET data. The uncorrected and corrected PET images were compared side-by-side, focusing on areas prone to movement artifacts. The assessment revealed that the motion correction successfully addressed minor head tilts and rotations, resulting in more stable and aligned images. This suggests that the motion correction method effectively minimized inter-frame patient motion artifacts, enhancing the overall quality of the PET data.

Similar studies have highlighted the importance of motion correction in PET imaging. For instance, Miranda et al. [47] demonstrated that rigid registration could significantly improve image quality in brain PET scans by reducing motion artifacts

[47]. The findings of this thesis consistent with these reports, reinforcing the efficacy of rigid registration for motion correction. However, unlike Wang et al.[91], who used additional quantitative metrics to evaluate alignment accuracy, the assessment of the implemented motion correction was limited to visual inspection [91].

While visual inspection provided initial insights into the effectiveness of motion correction, it is subjective. Future work should incorporate quantitative assessment methods, such as image similarity metrics or statistical analyses, to objectively measure the improvements in image alignment. Additionally, exploring advanced machine learning-based approaches, could further enhance the accuracy and robustness of the correction process [91], [92].

In this thesis, the selection of the reference frame, which is crucial for accurate alignment of the frames in motion correction processes, was performed manually. Traditionally, this involves choosing a frame from the early stages of the scan where the entire brain is visible and motion artifacts are minimal. However, manual selection can be subjective and potentially inconsistent.

To address the challenges of manually selecting the reference frame AI-driven techniques, particularly Generative Adversarial Networks (GANs) [92], could be used to automate and enhance the selection of optimal reference frames. An AI-generated reference frames could provide stable reference points for the entire motion correction pipeline, thus eliminating the need for manual selection of a reference frame [93].

Integrating AI-enhanced reference frames involves training a GAN to produce synthetic frames looking like late time frames from the early frames, which than can be used as reference frames [91], [92], [93], [94].

Employing AI to select reference frames to use for the motion correction pipeline has the potential to enhance clinical workflows by reducing the time and expertise needed to preprocess PET data. This advancement also paves the way for innovative research in automated image processing applicable to various imaging modalities. Future research might investigate the effectiveness of GAN-generated reference frames versus those selected manually, potentially establishing new standards for motion correction techniques in medical imaging [91], [92], [93], [94].

**Partial volume correction**

Traditional methods for determining the input function in PET imaging rely on arterial blood sampling, which is invasive and often impractical due to patient discomfort and the need for specialists. To address these challenges this thesis

adapted an image-derived input function (IDIF) with partial volume correction (PVC).

Partial volume effects (PVEs) arise from the limited spatial resolution of PET scanners, causing signal spillover between adjacent tissues and distorting tracer concentration measurements. This is particularly problematic in small structures like the carotid arteries. Correcting PVEs is crucial for reliability and accuracy of PET data [42].

The PVC approach implemented in this thesis adjusts for both spill-in and spill-out effects. By refining the signal within the PET data, PVC ensures that the measured tracer concentrations more accurately reflect their true distribution. This is particularly important for small structures where spillover effects are distinct.

The effect of PVC was evaluated through various methods, including time activity curves, peak activity analysis, box plots, and comparison of AUC values before and after correction with literature. The log-transformed AUC values were significantly higher post-correction, indicating successful adjustment for PVEs. A paired t-test further supported these findings, revealing a statistically significant difference ($p = 0.0238$) between the uncorrected and corrected values.

Using the FET007 patient as a case study, the following observations were made:

- AUC increased around 90%.
- Peak Activity increase around 50%.

These results underscore the impact of the correction procedure on measured tracer concentrations. Both Peak Activity and AUC were notably higher in the corrected TAC, highlighting the tracer concentration measurements post-correction.

An interesting observation was made with patient FET090, who displayed an unusual IDIF distribution with two peaks, both enhanced by PVC. The most likely reason is that the bolus was given too slowly or was not administered as a single bolus.

One primary challenge in this thesis was validating the accuracy and reliability of IDIF due to the absence of a direct ground truth, typically provided by invasive arterial blood sampling. By comparing AUC and Peak Activity metrics between the uncorrected and corrected IDIFs, the effectiveness of the corrections was assessed. This approach does not measure accuracy against a known standard directly, so the increase in AUC after correction was compared to similar studies.

Previous studies by Sundar et al. [42] and Sari et al. [90] have demonstrated the benefits of PVC in improving measurements accuracy. Consistent with these studies, this thesis found a substantial increase in AUC values following PVC. Sundar et al. reported an increase in AUC values post-correction of 80% [42], and Sari et al. reported an increase of 95% [90]. These findings align with those of this thesis, where the AUC value post-correction increased around 90-110%. The application of the PVC method in this thesis resulted in a substantial increase in the Area Under the Curve values, a little higher than reported in other studies. The increase in AUC values and peak activity values post-correction suggests that while the PVC method is effective in enhancing the sensitivity it may also be overcorrecting the values. Overcorrection can occur when the PVC method compensates too aggressively for partial volume effects, leading to artificially inflated AUC measurements.

Significant enhancements in IDIF, AUC measurements, and peak activity were observed, underscoring the effectiveness of the PVC methods implemented.

The peak activity values also show a notable increase after correction, with a median percentage increase of approximately 52.69%. However, there is considerable variability in the percentage increase of peak activity values across different patients. For instance, some patients exhibited increases as high as 134.85%, while others had more modest increases of around 32.59%.

This variability in peak activity enhancement suggests that individual patient characteristics play a significant role in the effectiveness of the correction method. Factors such as tissue composition, blood flow, and the extent of partial volume effects could contribute to these differences.

Overall, the correction method shows promise in improving the quantification of tracer uptake, but a deeper understanding of patient-specific responses will be essential for maximizing its use.

This research emphasizes the importance of spill-out and spill-in corrections in achieving more accurate IDIF values. As researchers continue to advance in this field, the insights gained here offer a foundation for enhanced patient care strategies and diagnostic methodologies.

Numerous studies have successfully implemented IDIFs in PET imaging; however, applications specific to 18F-FET are relatively sparse. The unique properties of 18F-FET, including its positron range and varying background activities, pose distinct challenges. Additionally, differences in algorithm convergence can impact

the accuracy of PVC and IDIF outcomes. Addressing these factors is crucial for optimizing IDIF implementation in 18F-FET PET studies.

The integration of IDIF, combined with motion correction and PVC, supports the hypothesis that non-invasive techniques can provide quantitatively accurate tracer concentration representations over time for kinetic modeling, eliminating the need for invasive arterial blood sampling. The observed increases in AUC and Peak Activity in the corrected datasets, compared to the uncorrected ones and with literature, confirm the hypothesis: “The developed Image-Derived Input Function and motion correction can provide quantitatively accurate representations of tracer concentrations over time for kinetic modeling, eliminating the need for invasive arterial blood sampling.” This work demonstrates the need of IDIF in kinetic modeling and highlights the substantial improvements in PET data accuracy through the implemented correction techniques.

Future studies might benefit from an expanded dataset as well as integrating data from both PET-CT and PET-MRI examinations. Exploring other correction methods or computational models may further refine the accuracy of IDIF values.

This master's thesis encountered unexpected challenges which posed limitations. The study group size was shortened by the exclusion of a specific PET-data set, namely FET005. This particular dataset was rendered unusable due to a delay in initiating the dynamic 18F-FET PET MRI scan, causing the initial tracer uptake to be missed. This initial uptake is imperative for IDIF as it showcases the immediate kinetics of the tracer following injection. The very first moments post-injection are critical as they represent the tracer's maximum bloodstream concentration. This peak is crucial for ensuing accurate pharmacokinetic modeling because it is shedding light on the tracer's initial distribution volume. Furthermore, the early phase of uptake typically benefits from the finest temporal resolution in dynamic PET studies, spotlighting the brisk kinetics of tracer dispersion. In essence, the absence of this initial uptake phase means the IDIF is without comprehensive data about the tracer's full body dynamics, which could culminate in inaccurate interpretations or potentially flawed modeling results.

One of the primary limitations of this study, alongside page constraints, was the limited time available for comprehensive testing and implementation. This time limitation particularly impacted the application of the motion correction and spillover correction techniques developed in this thesis. While these techniques were successfully integrated into Poglitsch's existing script, due to time constraints, only the initial part of the script could be executed. The complete processing of a single patient dataset using Poglitsch's script takes an extensive duration—approximately 4-6 hours. This underscores the necessity for further research to thoroughly assess

the effectiveness of these enhancements in the context of the complete script and larger patient datasets.

The scope of this master's thesis is inherently limited, given the constraints of time, resources, and the depth required for a project of this academic level. While a more extensive exploration could provide additional insights, it would surpass the boundaries set for a master's-level investigation. Recognizing this constraint is important as it is a limitation of the current study. Nonetheless, this thesis serves as a foundation and starting point for further investigation within a dissertation or more expansive research, where there may be fewer resource limitations.

In the era of increasing integration of machine learning and artificial intelligence within the realm of medical imaging, the significance of having well-defined, consistent metrics like IDIF is vital. These metrics serve as structured data points that can be seamlessly incorporated into algorithms for a multitude of applications, including predictive modeling, treatment strategy development, and patient classification. Such standardized metrics become a cornerstone in the quest for precision and personalized healthcare solutions.

In essence, the IDIF is crucial in 18F-FET PET/MRI glioma scans because it supports quantitative analysis, allows for dynamic imaging insights, aids in tumor characterization and monitoring, and provides a non-invasive and patient-friendly approach to obtaining essential data.

# 6 Conclusion

Despite the limitations, this study has demonstrated that IDIFs used for FDG can potentially be used for tracers with different uptake patterns. The main goal of this thesis was to integrate motion correction and a quantitatively accurate partial volume correction technique to advance quantitative accuracy in kinetic modeling, specifically for image-derived input-function extraction. Hence, the time-sensitive activity concentration in the tissue adjacent to the carotid arteries was evaluated, leading to the development of a spillover correction that is both time and tissue dependent.

The Hypothesis for this project was:

“The developed Image-Derived Input Function and motion correction can provide quantitatively accurate representations of tracer concentrations over time for kinetic modeling, eliminating the need for invasive arterial blood sampling.”

Based on the findings and analyses conducted throughout this project, the hypothesis was validated. The integrated motion correction and Image-Derived Input Function provide quantitatively accurate representations of tracer concentrations over time for kinetic modeling. This confirms the possibility of eliminating the need for invasive arterial blood sampling, aligning with the initial hypothesis.

While the PVC method used in this thesis significantly improves the quantification of tracer uptake, the potential for overcorrection should be carefully considered.

In conclusion, the results of this study suggest a promising future for the use of a quantitatively accurate IDIF. Arterial blood sampling, which is invasive and can be uncomfortable for the patient, would not be necessary anymore. Moreover, a quantitative approach ensures consistent and reproducible measurements, which is essential in clinical and research settings.

# References


[1] D. N. Louis *et al.*, “The 2016 World Health Organization Classification of Tumors of the Central Nervous System: a summary,” *Acta Neuropathol*, vol. 131, no. 6, pp. 803–820, Jun. 2016, doi: 10.1007/s00401-016-1545-1.

[2] G. Schwarzmüller-Erber, E. Silberstein, and S. Eder, *Angewandte Magnetresonanztomographie: Grundlagen und Anwendungen*, 2nd ed., vol. 2. Vienna: Facultas, 2012.

[3] N. Upadhyay and A. D. Waldman, “Conventional MRI evaluation of gliomas.,” *Br J Radiol*, vol. 84 Spec No 2, no. Spec Iss 2, pp. S107-11, Dec. 2011, doi: 10.1259/bjr/65711810.

[4] N. L. Jansen *et al.*, “Prognostic significance of dynamic 18F-FET PET in newly diagnosed astrocytic high-grade glioma.,” *J Nucl Med*, vol. 56, no. 1, pp. 9–15, Jan. 2015, doi: 10.2967/jnumed.114.144675.

[5] A. Tatkovic, R. McBean, E. Perkins, and D. Wong, “18 F-FET PET maximum standard uptake value and WHO tumour classification grade in glioma.,” *J Med Imaging Radiat Oncol*, vol. 66, no. 3, pp. 332–336, Apr. 2022, doi: 10.1111/1754-9485.13322.

[6] N. Galldiks *et al.*, “The use of dynamic O-(2-18F-fluoroethyl)-l-tyrosine PET in the diagnosis of patients with progressive and recurrent glioma.,” *Neuro Oncol*, vol. 17, no. 9, pp. 1293–300, Sep. 2015, doi: 10.1093/neuonc/nov088.

[7] Matthias Hannes Poglitsch, “Kinetische Modellierung bei dynamischen 18F-FET-PET Untersuchungen von Gliomen,” Medizinischen Universität Wien, Vienna, 20AD.

[8] M. Röhrich *et al.*, “Integrated analysis of dynamic FET PET/CT parameters, histology, and methylation profiling of 44 gliomas.,” *Eur J Nucl Med Mol Imaging*, vol. 45, no. 9, pp. 1573–1584, Jul. 2018, doi: 10.1007/s00259-018-4009-0.

[9] S. Brandner *et al.*, “Diagnostic accuracy of 1p/19q codeletion tests in oligodendroglioma: A comprehensive meta-analysis based on a Cochrane

systematic review," *Neuropathol Appl Neurobiol*, vol. 48, no. 4, Jun. 2022, doi: 10.1111/nan.12790.

[10] Schwarz Thomas and Tiutin Leonid, *Positron Emission Tomography*. New Delhi: Springer India, 2015. doi: 10.1007/978-81-322-2098-5.

[11] G. Hevesy, "The Absorption and Translocation of Lead by Plants," *Biochemical Journal*, vol. 17, no. 4–5, pp. 439–445, Jan. 1923, doi: 10.1042/bj0170439.

[12] M. R. Kilbourn, "11C- and 18F-Radiotracers for In Vivo Imaging of the Dopamine System: Past, Present and Future," *Biomedicines*, vol. 9, no. 2, p. 108, Jan. 2021, doi: 10.3390/biomedicines9020108.

[13] M. Schou, V. Pike, and C. Halldin, "Development of Radioligands for Imaging of Brain Norepinephrine Transporters In Vivo with Positron Emission Tomography," *Curr Top Med Chem*, vol. 7, no. 18, pp. 1806–1816, Sep. 2007, doi: 10.2174/156802607782507411.

[14] Paul. A. Tipler, *Physik, für Wissenschaftler und Ingenieure*, 2nd ed. Heidelberg: Springer Berlin Heidelberg, 2007.

[15] David Jenkins, *Radiation Detection for Nuclear Physics: Methods and industrial applications*. IOP Publishing, 2020.

[16] Dale L Bailey, David W Townsend, Peter E Valk, and Michael N Maisey, *Positron Emission Tomography Basic Science* . 2005.

[17] T. Beyer *et al.*, "A combined PET/CT scanner for clinical oncology.," *J Nucl Med*, vol. 41, no. 8, pp. 1369–79, Aug. 2000.

[18] M.-A. Tetrault, J. F. Oliver, M. Bergeron, R. Lecomte, and R. Fontaine, "Real Time Coincidence Detection Engine for High Count Rate Timestamp Based PET," *IEEE Trans Nucl Sci*, vol. 57, no. 1, pp. 117–124, Feb. 2010, doi: 10.1109/TNS.2009.2038055.

[19] Lalith Kumar Shiyam Sundar, "Personalized neuroimaging for improved assessment of non-lesional epilepsy based on fully-integrated PET/MRI imaging," Medical University of Vienna, Vienna, 2019.

[20] T. E. Nichols, Jinyi Qi, E. Asma, and R. M. Leahy, "Spatiotemporal reconstruction of list-mode PET data," *IEEE Trans Med Imaging*, vol. 21, no. 4, pp. 396–404, Apr. 2002, doi: 10.1109/TMI.2002.1000263.

[21] K. Gong, K. Kim, J. Cui, D. Wu, and Q. Li, “The Evolution of Image Reconstruction in PET: From Filtered Back-Projection to Artificial Intelligence.,” *PET Clin*, vol. 16, no. 4, pp. 533–542, Oct. 2021, doi: 10.1016/j.cpet.2021.06.004.

[22] L. A. Shepp and Y. Vardi, “Maximum Likelihood Reconstruction for Emission Tomography,” *IEEE Trans Med Imaging*, vol. 1, no. 2, pp. 113–122, Oct. 1982, doi: 10.1109/TMI.1982.4307558.

[23] H. M. Hudson and R. S. Larkin, “Accelerated image reconstruction using ordered subsets of projection data,” *IEEE Trans Med Imaging*, vol. 13, no. 4, pp. 601–609, 1994, doi: 10.1109/42.363108.

[24] Ronald Boellaard, Adriaan A. Lammertsma, and Arthur van Lingen, “Experimental and Clinical Evaluation of Iterative Reconstruction (OSEM) in Dynamic PET: Quantitative Characteristics and Effects on Kinetic Modeling,” *Journal of Nuclear Medicine*, vol. 42, May 2001.

[25] H. Zaidi and W. D. Erwin, “Quantitative Analysis in Nuclear Medicine Imaging,” *Journal of Nuclear Medicine*, vol. 48, no. 8, pp. 1401–1401, Aug. 2007, doi: 10.2967/jnumed.107.042598.

[26] S. C. Huang, E. J. Hoffman, M. E. Phelps, and D. E. Kuhl, “Quantitation in positron emission computed tomography: 2. Effects of inaccurate attenuation correction.,” *J Comput Assist Tomogr*, vol. 3, no. 6, pp. 804–14, Dec. 1979.

[27] H. Ostertag, W. K. K□bler, J. Doll, and W. J. Lorenz, “Measured attenuation correction methods,” *Eur J Nucl Med*, vol. 15, no. 11, pp. 722–726, 1989, doi: 10.1007/BF00631764.

[28] P. E. Kinahan, D. W. Townsend, T. Beyer, and D. Sashin, “Attenuation correction for a combined 3D PET/CT scanner,” *Med Phys*, vol. 25, no. 10, pp. 2046–2053, Oct. 1998, doi: 10.1118/1.598392.

[29] J. P. J. Carney, D. W. Townsend, V. Rappoport, and B. Bendriem, “Method for transforming CT images for attenuation correction in PET/CT imaging,” *Med Phys*, vol. 33, no. 4, pp. 976–983, Mar. 2006, doi: 10.1118/1.2174132.

[30] C. N. Ladefoged *et al.*, “A multi-centre evaluation of eleven clinically feasible brain PET/MRI attenuation correction techniques using a large cohort of patients,” *Neuroimage*, vol. 147, pp. 346–359, Feb. 2017, doi: 10.1016/j.neuroimage.2016.12.010.

[31] D. L. Bailey *et al.*, “Combined PET/MRI: Global Warming—Summary Report of the 6th International Workshop on PET/MRI, March 27–29, 2017, Tübingen, Germany,” *Mol Imaging Biol*, vol. 20, no. 1, pp. 4–20, Feb. 2018, doi: 10.1007/s11307-017-1123-5.

[32] B. K. Das, Ed., *Positron Emission Tomography*. New Delhi: Springer India, 2015. doi: 10.1007/978-81-322-2098-5.

[33] C. C. Watson, M. E. Casey, C. Michel, and B. Bendriem, “Advances in scatter correction for 3D PET/CT,” in *IEEE Symposium Conference Record Nuclear Science 2004.*, IEEE, pp. 3008–3012. doi: 10.1109/NSSMIC.2004.1466317.

[34] Jeffrey D. Steinberg, “MRI-BASED ATTENUATION CORRECTION FOR PET RECONSTRUCTION,” Ohio, 2009.

[35] S. C. Huang, E. J. Hoffman, M. E. Phelps, and D. E. Kuhl, “Quantitation in positron emission computed tomography: 3 Effect of sampling.,” *J Comput Assist Tomogr*, vol. 4, no. 6, pp. 819–26, Dec. 1980, doi: 10.1097/00004728-198012000-00014.

[36] M. Soret, S. L. Bacharach, and I. Buvat, “Partial-Volume Effect in PET Tumor Imaging,” *Journal of Nuclear Medicine*, vol. 48, no. 6, pp. 932–945, Jun. 2007, doi: 10.2967/jnumed.106.035774.

[37] K. Erlandsson, K. Kacperski, D. van Gramberg, and B. F. Hutton, “Performance evaluation of D-SPECT: a novel SPECT system for nuclear cardiology,” *Phys Med Biol*, vol. 54, no. 9, pp. 2635–2649, May 2009, doi: 10.1088/0031-9155/54/9/003.

[38] D. D’Ambrosio, M. Marengo, S. Boschi, S. Fanti, and A. E. Spinelli, *Post-Reconstruction Partial Volume Correction of PET Images Using Iterative Deconvo- lution Algorithm and Anatomical Priors*. Munich, Germany: Springer Berlin Heidelberg, 2009.

[39] V. Y. Panin, F. Kehren, C. Michel, and M. Casey, “Fully 3-D PET reconstruction with system matrix derived from point source measurements,” *IEEE Trans Med Imaging*, vol. 25, no. 7, pp. 907–921, Jul. 2006, doi: 10.1109/TMI.2006.876171.

[40] M. I. Akerele *et al.*, “Comparison of Correction Techniques for the Spill in Effect in Emission Tomography.,” *IEEE Trans Radiat Plasma Med Sci*, vol. 4, no. 4, pp. 422–432, Jul. 2020, doi: 10.1109/TRPMS.2020.2980443.

[41] V. Bettinardi, I. Castiglioni, E. De Bernardi, and M. C. Gilardi, “PET quantification: strategies for partial volume correction,” *Clin Transl Imaging*, vol. 2, no. 3, pp. 199–218, Jun. 2014, doi: 10.1007/s40336-014-0066-y.

[42] L. K. Sundar *et al.*, “Towards quantitative [18F]FDG-PET/MRI of the brain: Automated MR-driven calculation of an image-derived input function for the non-invasive determination of cerebral glucose metabolic rates,” *Journal of Cerebral Blood Flow & Metabolism*, vol. 39, no. 8, pp. 1516–1530, Aug. 2019, doi: 10.1177/0271678X18776820.

[43] J. E. M. Mourik *et al.*, “Image derived input functions for dynamic High Resolution Research Tomograph PET brain studies,” *Neuroimage*, vol. 43, no. 4, pp. 676–686, Dec. 2008, doi: 10.1016/j.neuroimage.2008.07.035.

[44] T. Sun *et al.*, “Motion correction and its impact on quantification in dynamic total-body 18F-fluorodeoxyglucose PET,” *EJNMMI Phys*, vol. 9, no. 1, p. 62, Sep. 2022, doi: 10.1186/s40658-022-00493-9.

[45] C. Catana, “Motion correction options in PET/MRI.,” *Semin Nucl Med*, vol. 45, no. 3, pp. 212–23, May 2015, doi: 10.1053/j.semnuclmed.2015.01.001.

[46] L. K. Shiyam Sundar *et al.*, “Fully Automated, Fast Motion Correction of Dynamic Whole-Body and Total-Body PET/CT Imaging Studies.,” *J Nucl Med*, vol. 64, no. 7, pp. 1145–1153, Jul. 2023, doi: 10.2967/jnumed.122.265362.

[47] A. Miranda, T. Kroll, V. Schweda, S. Staelens, and J. Verhaeghe, “Correction of motion tracking errors for PET head rigid motion correction,” *Phys Med Biol*, vol. 68, no. 17, p. 175009, Sep. 2023, doi: 10.1088/1361-6560/acec2c.

[48] T. J. Dolan, Ed., *Magnetic Fusion Technology*, vol. 19. London: Springer London, 2013. doi: 10.1007/978-1-4471-5556-0.

[49] M. Filippi, Ed., *fMRI Techniques and Protocols*, vol. 119. New York, NY: Springer New York, 2016. doi: 10.1007/978-1-4939-5611-1.

[50] D. Weishaupt, V. D. Köchli, and B. Marincek, *Wie funktioniert MRI?* Berlin, Heidelberg: Springer Berlin Heidelberg, 2014. doi: 10.1007/978-3-642-41616-3.

[51] S. Vandenberghe and P. K. Marsden, “PET-MRI: a review of challenges and solutions in the development of integrated multimodality imaging.,” *Phys Med Biol*, vol. 60, no. 4, pp. R115-54, Feb. 2015, doi: 10.1088/0031-9155/60/4/R115.

[52] H. F. Wehrl, A. W. Sauter, M. S. Judenhofer, and B. J. Pichler, “Combined PET/MR Imaging — Technology and Applications,” *Technol Cancer Res Treat*, vol. 9, no. 1, pp. 5–20, Feb. 2010, doi: 10.1177/153303461000900102.

[53] M. S. Judenhofer *et al.*, “Simultaneous PET-MRI: a new approach for functional and morphological imaging,” *Nat Med*, vol. 14, no. 4, pp. 459–465, Apr. 2008, doi: 10.1038/nm1700.

[54] H. Zaidi *et al.*, “Design and performance evaluation of a whole-body Ingenuity TF PET–MRI system,” *Phys Med Biol*, vol. 56, no. 10, pp. 3091–3106, May 2011, doi: 10.1088/0031-9155/56/10/013.

[55] S. I. Ziegler *et al.*, “A prototype high-resolution animal positron tomograph with avalanche photodiode arrays and LSO crystals,” *Eur J Nucl Med*, vol. 28, no. 2, pp. 136–143, Feb. 2001, doi: 10.1007/s002590000438.

[56] J. Wehner *et al.*, “PET/MRI insert using digital SiPMs: Investigation of MR-compatibility,” *Nucl Instrum Methods Phys Res A*, vol. 734, pp. 116–121, Jan. 2014, doi: 10.1016/j.nima.2013.08.077.

[57] G. Delso *et al.*, “Performance Measurements of the Siemens mMR Integrated Whole-Body PET/MR Scanner,” *Journal of Nuclear Medicine*, vol. 52, no. 12, pp. 1914–1922, Dec. 2011, doi: 10.2967/jnumed.111.092726.

[58] C. S. Levin, S. H. Maramraju, M. M. Khalighi, T. W. Deller, G. Delso, and F. Jansen, “Design Features and Mutual Compatibility Studies of the Time-of-Flight PET Capable GE SIGNA PET/MR System,” *IEEE Trans Med Imaging*, vol. 35, no. 8, pp. 1907–1914, Aug. 2016, doi: 10.1109/TMI.2016.2537811.

[59] J. Cal-Gonzalez *et al.*, “Hybrid Imaging: Instrumentation and Data Processing,” *Front Phys*, vol. 6, May 2018, doi: 10.3389/fphy.2018.00047.

[60] N. Burgos *et al.*, “Attenuation Correction Synthesis for Hybrid PET-MR Scanners: Application to Brain Studies,” *IEEE Trans Med Imaging*, vol. 33, no. 12, pp. 2332–2341, Dec. 2014, doi: 10.1109/TMI.2014.2340135.

[61] N. Burgos *et al.*, “Multi-contrast attenuation map synthesis for PET/MR scanners: assessment on FDG and Florbetapir PET tracers,” *Eur J Nucl Med Mol Imaging*, vol. 42, no. 9, pp. 1447–1458, Aug. 2015, doi: 10.1007/s00259-015-3082-x.

[62] A. P. Leynes *et al.*, “Hybrid ZTE/Dixon MR-based attenuation correction for quantitative uptake estimation of pelvic lesions in PET/MRI,” *Med Phys*, vol. 44, no. 3, pp. 902–913, Mar. 2017, doi: 10.1002/mp.12122.

[63] G. Wagenknecht, H.-J. Kaiser, F. M. Mottaghy, and H. Herzog, “MRI for attenuation correction in PET: methods and challenges,” *Magnetic Resonance Materials in Physics, Biology and Medicine*, vol. 26, no. 1, pp. 99–113, Feb. 2013, doi: 10.1007/s10334-012-0353-4.

[64] C. N. Ladefoged *et al.*, “Region specific optimization of continuous linear attenuation coefficients based on UTE (RESOLUTE): application to PET/MR brain imaging,” *Phys Med Biol*, vol. 60, no. 20, pp. 8047–8065, Oct. 2015, doi: 10.1088/0031-9155/60/20/8047.

[65] B. Fei *et al.*, “MR/PET quantification tools: Registration, segmentation, classification, and MR-based attenuation correction,” *Med Phys*, vol. 39, no. 10, pp. 6443–6454, Oct. 2012, doi: 10.1118/1.4754796.

[66] H. Zaidi, M.-L. Montandon, and D. O. Slosman, “Magnetic resonance imaging-guided attenuation and scatter corrections in three-dimensional brain positron emission tomography,” *Med Phys*, vol. 30, no. 5, pp. 937–948, Apr. 2003, doi: 10.1118/1.1569270.

[67] C. Catana *et al.*, “Toward Implementing an MRI-Based PET Attenuation-Correction Method for Neurologic Studies on the MR-PET Brain Prototype,” *Journal of Nuclear Medicine*, vol. 51, no. 9, pp. 1431–1438, Sep. 2010, doi: 10.2967/jnumed.109.069112.

[68] K. Gong, J. Yang, K. Kim, G. El Fakhri, Y. Seo, and Q. Li, “Attenuation correction for brain PET imaging using deep neural network based on Dixon and ZTE MR images,” *Phys Med Biol*, vol. 63, no. 12, p. 125011, Jun. 2018, doi: 10.1088/1361-6560/aac763.

[69] X. Han, “MR-based synthetic CT generation using a deep convolutional neural network method,” *Med Phys*, vol. 44, no. 4, pp. 1408–1419, Apr. 2017, doi: 10.1002/mp.12155.

[70] J. Nuyts, P. Dupont, S. Stroobants, R. Benninck, L. Mortelmans, and P. Suetens, “Simultaneous maximum a posteriori reconstruction of attenuation and activity distributions from emission sinograms,” *IEEE Trans Med Imaging*, vol. 18, no. 5, pp. 393–403, May 1999, doi: 10.1109/42.774167.

[71] A. Mehranian, H. Zaidi, and A. J. Reader, “MR-guided joint reconstruction of activity and attenuation in brain PET-MR,” *Neuroimage*, vol. 162, pp. 276–288, Nov. 2017, doi: 10.1016/j.neuroimage.2017.09.006.

[72] N. H. Clinthorne, J. A. Fessler, G. D. Hutchins, and W. L. Rogers, “Joint maximum likelihood estimation of emission and attenuation densities in PET,” in *Conference Record of the 1991 IEEE Nuclear Science Symposium and Medical Imaging Conference*, IEEE, pp. 1927–1932. doi: 10.1109/NSSMIC.1991.259253.

[73] A. Martinez-Möller *et al.*, “Tissue Classification as a Potential Approach for Attenuation Correction in Whole-Body PET/MRI: Evaluation with PET/CT Data,” *Journal of Nuclear Medicine*, vol. 50, no. 4, pp. 520–526, Apr. 2009, doi: 10.2967/jnumed.108.054726.

[74] A. K. P. E. G. A. H. S. S. U.-M. F. and L. E. Lars Birger Aasheim, “ET/MR brain imaging: evaluation of clinical UTE-based attenuation correction,” *European Journal of Nuclear Medicine and Molec- ular Imaging*, vol. 42, no. 1439–1446, Aug. 2015.

[75] T. Koesters *et al.*, “Dixon Sequence with Superimposed Model-Based Bone Compartment Provides Highly Accurate PET/MR Attenuation Correction of the Brain,” *Journal of Nuclear Medicine*, vol. 57, no. 6, pp. 918–924, Jun. 2016, doi: 10.2967/jnumed.115.166967.

[76] I. Law *et al.*, “Joint EANM/EANO/RANO practice guidelines/SNMMI procedure standards for imaging of gliomas using PET with radiolabelled amino acids and [18F]FDG: version 1.0.,” *Eur J Nucl Med Mol Imaging*, vol. 46, no. 3, pp. 540–557, Mar. 2019, doi: 10.1007/s00259-018-4207-9.

[77] A. Verger *et al.*, “Comparison of 18F-FET PET and perfusion-weighted MRI for glioma grading: a hybrid PET/MR study.,” *Eur J Nucl Med Mol Imaging*, vol. 44, no. 13, pp. 2257–2265, Dec. 2017, doi: 10.1007/s00259-017-3812-3.

[78] F. J. Vettermann *et al.*, “Characterization of Diffuse Gliomas With Histone H3-G34 Mutation by MRI and Dynamic 18F-FET PET,” *Clin Nucl Med*, vol. 43, no. 12, pp. 895–898, Dec. 2018, doi: 10.1097/RLU.0000000000002300.

[79] N. Galldiks *et al.*, “Role of O-(2-18F-fluoroethyl)-L-tyrosine PET as a diagnostic tool for detection of malignant progression in patients with low-grade glioma.,” *J Nucl Med*, vol. 54, no. 12, pp. 2046–54, Dec. 2013, doi: 10.2967/jnumed.113.123836.

[80] N. Galldiks *et al.*, “Role of O-(2-(18)F-fluoroethyl)-L-tyrosine PET for differentiation of local recurrent brain metastasis from radiation necrosis.,” *J Nucl Med*, vol. 53, no. 9, pp. 1367–74, Sep. 2012, doi: 10.2967/jnumed.112.103325.

[81] C. Debus *et al.*, “Feasibility and robustness of dynamic 18F-FET PET based tracer kinetic models applied to patients with recurrent high-grade glioma prior to carbon ion irradiation.,” *Sci Rep*, vol. 8, no. 1, p. 14760, Oct. 2018, doi: 10.1038/s41598-018-33034-5.

[82] S. Schön *et al.*, “Imaging glioma biology: spatial comparison of amino acid PET, amide proton transfer, and perfusion-weighted MRI in newly diagnosed gliomas.,” *Eur J Nucl Med Mol Imaging*, vol. 47, no. 6, pp. 1468–1475, Jun. 2020, doi: 10.1007/s00259-019-04677-x.

[83] N. Verburg *et al.*, “Improved detection of diffuse glioma infiltration with imaging combinations: a diagnostic accuracy study.,” *Neuro Oncol*, vol. 22, no. 3, pp. 412–422, Mar. 2020, doi: 10.1093/neuonc/noz180.

[84] P. Blanc-Durand *et al.*, “Voxel-based 18F-FET PET segmentation and automatic clustering of tumor voxels: A significant association with IDH1 mutation status and survival in patients with gliomas,” *PLoS One*, vol. 13, no. 6, p. e0199379, Jun. 2018, doi: 10.1371/journal.pone.0199379.

[85] K. J. Paprottka *et al.*, “Fully automated analysis combining [18F]-FET-PET and multiparametric MRI including DSC perfusion and APTw imaging: a promising tool for objective evaluation of glioma progression.,” *Eur J Nucl Med Mol Imaging*, vol. 48, no. 13, pp. 4445–4455, Dec. 2021, doi: 10.1007/s00259-021-05427-8.

[86] J. Bolcaen *et al.*, “Kinetic Modeling and Graphical Analysis of 18F-Fluoromethylcholine (FCho), 18F-Fluoroethyltyrosine (FET) and 18F-Fluorodeoxyglucose (FDG) PET for the Fiscrimination between High-Grade Glioma and Radiation Necrosis in Rats.,” *PLoS One*, vol. 11, no. 8, p. e0161845, 2016, doi: 10.1371/journal.pone.0161845.

[87] M. A. Richard, J. P. Fouquet, R. Lebel, and M. Lepage, “Determination of an Optimal Pharmacokinetic Model of 18F-FET for Quantitative Applications in Rat Brain Tumors.,” *J Nucl Med*, vol. 58, no. 8, pp. 1278–1284, Aug. 2017, doi: 10.2967/jnumed.116.180612.

[88] T. Koopman *et al.*, “Quantification of O-(2-[18F]fluoroethyl)-L-tyrosine kinetics in glioma.,” *EJNMMI Res*, vol. 8, no. 1, p. 72, Jul. 2018, doi: 10.1186/s13550-018-0418-0.

[89] V. S. Vassiliadis and R. Conejeros, “Powell Method,” in *Encyclopedia of Optimization*, Boston, MA: Springer US, 2001, pp. 2001–2003. doi: 10.1007/0-306-48332-7_393.

[90] H. Sari *et al.*, “Estimation of an image derived input function with MR-defined carotid arteries in FDG-PET human studies using a novel partial volume correction method,” *Journal of Cerebral Blood Flow & Metabolism*, vol. 37, no. 4, pp. 1398–1409, Apr. 2017, doi: 10.1177/0271678X16656197.

[91] J. Wang *et al.*, “Motion correction strategies for enhancing whole-body PET imaging,” *Frontiers in Nuclear Medicine*, vol. 4, Feb. 2024, doi: 10.3389/fnume.2024.1257880.

[92] M. Wenzel, “Generative Adversarial Networks and Other Generative Models,” 2023, pp. 139–192. doi: 10.1007/978-1-0716-3195-9_5.

[93] B. L. Vey, J. W. Gichoya, A. Prater, and C. M. Hawkins, “The Role of Generative Adversarial Networks in Radiation Reduction and Artifact Correction in Medical Imaging,” *Journal of the American College of Radiology*, vol. 16, no. 9, pp. 1273–1278, Sep. 2019, doi: 10.1016/j.jacr.2019.05.040.

[94] X. Guo *et al.*, “TAI-GAN: Temporally and Anatomically Informed GAN for Early-to-Late Frame Conversion in Dynamic Cardiac PET Motion Correction,” 2023, pp. 64–74. doi: 10.1007/978-3-031-44689-4_7.

# List of Figures

# List of Tables

# Appendix

## A. Code

**Motion correction**

```
# import packages
import SimpleITK as sitk
import numpy as np
import nibabel as nib
import os
import argparse
from scipy.ndimage import affine_transform
from scipy.optimize import minimize


def rigid_registration(fixed, moving):
    """Perform rigid registration using optimization."""
    #funcitno uses fixed and moving image

    def cost_function(params):
        # Extract parameters ( how well the moving image alings with the
fixed image based on translation and rotation )
        dx, dy, dz, theta_x, theta_y, theta_z = params

        # Rotation matrices for x, y, z axes
        Rx = np.array([[1, 0, 0],
                       [0, np.cos(theta_x), -np.sin(theta_x)],
                       [0, np.sin(theta_x), np.cos(theta_x)]])
        # creates matrix Rx for rotating the image around the x-axis by
theta_x radians.
        #The rotation affects the y and z components but leaves the x
component unchanged.
        Ry = np.array([[np.cos(theta_y), 0, np.sin(theta_y)],
                       [0, 1, 0],
                       [-np.sin(theta_y), 0, np.cos(theta_y)]])
        #Ry matrix for rotating around the y-axis by theta_y radians.
        #This rotation affects the x and z components while leaving the y
component unchanged.
        Rz = np.array([[np.cos(theta_z), -np.sin(theta_z), 0],
                       [np.sin(theta_z), np.cos(theta_z), 0],
                       [0, 0, 1]])
        #Rz matrix around the z-axis by theta_z radians.
        #This affects the x and y components but not the z component.
        R = np.dot(Rz, np.dot(Ry, Rx))
```

```
        #Combined rotation matrix
        #will apply all three rotations in sequence: first around the x-
axis, then the y-axis, and finally the z-axis
        transformed = affine_transform(moving, R, offset=(
            dx, dy, dz), order=1, mode='constant')
        #This applies the combined rotation (R) and translation (dx, dy,
dz) to the moving image.
        #result  a version of the moving image that has been shifted and
rotated.
        # Cost is the negative cross-correlation
        return -np.sum(fixed * transformed)
        #returns negative of the sum of the element-wise multiplication
of the fixed and transformed images. a measure of similarity;
        # by minimizing this value, the algorithm maximizes the alignment
between the two images.
    initial_params = [0, 0, 0, 0, 0, 0]
    # starting points for optimazation
    result = minimize(cost_function, initial_params, method='Powell')
    #optimization method (Powell's method)  is used to find the best set
of parameters (rotations and translations)
    #that minimize the cost function - that best align the moving image
to the fixed one

    return result.x
    #returns optimal parameters

def apply_transformation(image, params):
    """Apply the rigid transformation to an image."""
    dx, dy, dz, theta_x, theta_y, theta_z = params
    #unpacks transformation param.
    #rotation matrices
    Rx = np.array([[1, 0, 0],
                   [0, np.cos(theta_x), -np.sin(theta_x)],
                   [0, np.sin(theta_x), np.cos(theta_x)]])
    Ry = np.array([[np.cos(theta_y), 0, np.sin(theta_y)],
                   [0, 1, 0],
                   [-np.sin(theta_y), 0, np.cos(theta_y)]])
    Rz = np.array([[np.cos(theta_z), -np.sin(theta_z), 0],
                   [np.sin(theta_z), np.cos(theta_z), 0],
                   [0, 0, 1]])
    R = np.dot(Rz, np.dot(Ry, Rx))
    #combines all three matrices into one that encapsulates the total
rotation effect (first rotating around the X-axis, then the Y-axis, and
finally the Z-axis)
    return affine_transform(image, R, offset=(dx, dy, dz), order=1,
mode='constant')
```

```
    """
    affine_transform -> function from SciPy that applies the affine
transformation to the image
    image: The original image data thath will be transformed
    R: The combined rotation matrix
    offset: The translation amounts (dx, dy, dz) that shift the image in
space
    order=1: This specifies bilinear interpolation for resampling (which
affects how the values between pixels are calculated during the
transformation)
    mode='constant': This sets how the function handles borders, it will
fill with constant values (defaults to zero) outside the boundaries of
the input
    """

def motion_correction_4d(data_4d, affine, output_path, start_frame):
    # Total number of frames
    total_frames = data_4d.shape[3]
    print(f"Total number of frames: {total_frames}")

    # Set the reference frame from a specified time after the initial
unstable period
    reference_frame = data_4d[:, :, :, start_frame]

    # Initialize a new array for the motion corrected data (empty array
same size ad data_4d)
    corrected_data = np.zeros_like(data_4d)

    # Process each frame
    for i in range(start_frame, total_frames):
        frame = data_4d[:, :, :, i]
        print(f"Processing frame {i+1} of {total_frames}")

        if i == start_frame:
            corrected_data[:, :, :, i] = frame
        else:
            params = rigid_registration(reference_frame, frame)
            corrected_frame = apply_transformation(frame, params)
            corrected_data[:, :, :, i] = corrected_frame

    """
    loops through each frame
    if  current frame is  middle frame it's copied directly into the
corrected_data array without changes
    all other frames rigid_registration function is called to find the
optimal transformation parameters that align this frame to the reference
frame
```

```
     apply_transformation is used to apply this calculated
transformation, and the corrected frame is stored in corrected_data
    """

    # Save the motion-corrected data as a new NIfTI file
    corrected_nifti = nib.Nifti1Image(corrected_data, affine)
    nib.save(corrected_nifti, output_path)

    print("Motion correction process completed.")


# Load the 4D NIfTI image
print('Reading Nifti:')
nifti_path =
'/Volumes/SSD/Matthias/Matthias_FET_PatData/FET090/Result/FET090_1x1_leas
t_square_minustime_0_whole_PET.nii'

# Load the NIfTI file
data, affine = load_nifti_4d(nifti_path)
print('NIfTI file loaded successfully.')

# Define the start frame based on PET data
start_frame = 10  # Example: start from the 10th frame
# Perform motion correction
print('MoCo starting')
output_path =
'/Volumes/SSD/Matthias/Matthias_FET_PatData/FET090/corrected_PET.nii'
motion_correction_4d(data, affine, output_path, start_frame)

print('MoCo finished')
print("Motion correction completed and saved to:", output_path)


# ============================
# Motion correction End
# ============================
```

**Partial Volume Correction:**

```
import numpy as np
from scipy.ndimage import gaussian_filter, binary_dilation,
generate_binary_structure
from skimage.filters import threshold_otsu
import nibabel as nib
import SimpleITK as sitk
import scipy as scp
```

```
def calculate_psfSigma(VOXEL_SIZE, PSF_FWHM):
    # Convert PSF_FWHM to an array if it is a scalar
    if np.isscalar(PSF_FWHM):
        PSF_FWHM = np.array([PSF_FWHM] * len(VOXEL_SIZE))
    else:
        psfFWHM = np.array(PSF_FWHM)
    psfFWHM /= np.array(VOXEL_SIZE)
    # Calculate the PSF sigma
    psfSigma = PSF_FWHM / np.sqrt(8 * np.log(2))
    return psfSigma.tolist()

def apply_psf_to_mask(mask, psf_sigma):
    # Apply Gaussian filter to mask to create spill out zone
    spill_out_zone = gaussian_filter(mask.astype(float), sigma=psf_sigma)
    return spill_out_zone

def create_background_mantel(spill_in_zone, dilation_size_mm,
VOXEL_SIZE):
    # Convert dilation size to pixels
    dilation_pixels = [int(dilation_size_mm / vs) for vs in VOXEL_SIZE]
    # Create a structural element for binary dilation
    struct_elem = generate_binary_structure(3, 1)
    # Perform binary dilation on the spill in zone
    dilated_zone = binary_dilation(spill_in_zone > 0.5,
structure=struct_elem, iterations=max(dilation_pixels))
    # Create background mantel by subtracting spill in zone from dilated
zone
    background_mantel = dilated_zone & ~ (spill_in_zone > 0.5)
    return background_mantel

def segment_background_mantel(pet_volume, background_mantel):
    # Get the activity in the background mantel
    mantel_activity = pet_volume[background_mantel]
    # Segment the background mantel using Otsu's threshold if activity is
present
    if np.any(mantel_activity):
        otsu_thresh = threshold_otsu(mantel_activity)
        segmented_mantel = (pet_volume > otsu_thresh) & background_mantel
    else:
        segmented_mantel = np.zeros_like(pet_volume, dtype=bool)
    return segmented_mantel

def spill_correction_volume(pet_data, carotid_mask_4d, VOXEL_SIZE,
PSF_FWHM, num_iter=10, epsilon=1e-5):
    # Calculate PSF sigma
    psfSigma = calculate_psfSigma(VOXEL_SIZE, PSF_FWHM)
    corrected_pet = pet_data.copy()
```

```
    # Define neighbor kernel for dilation
    neighbor_kernel = np.ones((3, 3, 3), dtype=int)
    neighbor_kernel[1, 1, 1] = 0

    for iteration in range(num_iter):
        print(f"Iteration {iteration + 1} of {num_iter}")
        PET_prev = corrected_pet.copy()
        for t in range(pet_data.shape[-1]):
            # Apply PSF to mask
            spill_out_zone = apply_psf_to_mask(carotid_mask_4d[..., t],
psfSigma)
            # Calculate spill out
            spill_out = gaussian_filter(corrected_pet[..., t] *
spill_out_zone, sigma=psfSigma)
            # Create immediate neighbors and background mantel
            immediate_neighbors = binary_dilation(carotid_mask_4d[...,
t], structure=neighbor_kernel) & ~carotid_mask_4d[..., t]
            background_mantel =
create_background_mantel(immediate_neighbors, 10, VOXEL_SIZE)
            segmented_mantel = segment_background_mantel(pet_data[...,
t], background_mantel)
            # Calculate spill in
            spill_in = gaussian_filter(corrected_pet[..., t] *
segmented_mantel, sigma=psfSigma)
            # Correct PET data
            corrected_pet[..., t] -= spill_out
            corrected_pet[..., t] += spill_in
        # Check for convergence
        if np.linalg.norm(corrected_pet - PET_prev) /
np.linalg.norm(PET_prev) < epsilon:
            print(f"Convergence reached at iteration {iteration + 1}")
            break
    return corrected_pet

def extract_tac(pet_data, mask):
    # Get indices of the mask
    mask_indices = np.where(mask)
    if pet_data.ndim == 4:
        num_time_frames = pet_data.shape[-1]
        tac = np.zeros(num_time_frames)
        # Calculate the mean activity in the mask for each time frame
        for t in range(num_time_frames):
            tac[t] = np.nanmean(pet_data[mask_indices[0],
mask_indices[1], mask_indices[2], t])
    elif pet_data.ndim == 3:
        tac = np.nanmean(pet_data[mask_indices])
    else:
```

```
        raise ValueError("Unexpected number of dimensions in pet_data.")
    return tac

def apply_positron_range_correction(pet_data, positron_range_mm,
voxel_size):
    # Calculate the sigma in voxels
    sigma_voxels = positron_range_mm / np.array(voxel_size)
    # Apply Gaussian filter to correct positron range
    corrected_data = gaussian_filter(pet_data, sigma=sigma_voxels)
    return corrected_data

# Load PET data
pet_file =
"/Volumes/SSD/Matthias/Matthias_FET_PatData/FET007/Result/FET007_1x1_leas
t_square_minustime_0_whole_PET.nii"
carotid_mask_file =
"/Volumes/SSD/Matthias/Matthias_FET_PatData/FET007/Result/FET007_1x1_leas
t_square_minustime_0_Carotis_registered.nii"
VOXEL_SIZE = [2.08626, 2.08626, 2.08626]
PSF_FWHM = [4.6, 5.0, 4.0]
POSITRON_RANGE_MM = 2.0

# Load PET data
pet_img = nib.load(pet_file)
pet_data = pet_img.get_fdata()
print("PET data shape: ", pet_data.shape)

# Load Carotid mask
carotid_mask_img = nib.load(carotid_mask_file)
carotid_mask_unshaped = carotid_mask_img.get_fdata().astype(np.int16)
print("Shape of Carotid_mask before adding dimension:",
carotid_mask_unshaped.shape)

# Expand carotid mask dimensions to match PET data
carotid_mask_4d = np.expand_dims(carotid_mask_unshaped, axis=-1)
carotid_mask_4d = np.repeat(carotid_mask_4d, pet_data.shape[3], axis=-1)
print("Shape of Carotid_mask with expand", carotid_mask_4d.shape)

# Extract IDIF from uncorrected data
print("Calculating IDIF from the uncorrected data")
stat_filter = sitk.LabelStatisticsImageFilter()
mean_vals = list()
mean_vals.append(0.0)
for t in range(pet_data.shape[-1]):
    pet_slice = pet_data[..., t]
    pet_slice_sitk = sitk.GetImageFromArray(pet_slice)
    carotid_mask_sitk = sitk.GetImageFromArray(carotid_mask_unshaped)
```

```
    stat_filter.Execute(pet_slice_sitk, carotid_mask_sitk)
    mean_v = stat_filter.GetMean(1)
    mean_vals.append(mean_v)

# Interpolate IDIF for uncorrected data
time_frames = list(range(pet_data.shape[-1] + 1))
x_list = time_frames
x_end = int(x_list[-1])
xnew = np.linspace(0, x_end, num=(int(x_end + 1)), endpoint=True)
xnew = xnew.astype('int16')

f1 = scp.interpolate.interp1d(x_list, mean_vals)
i_new = f1(xnew)

idif_uncorrected = np.array(i_new).astype('float32')

# PVC with Positron Range Correction
print("Starting with Positron Range Correction and PVC")
positron_range_corrected_pet = np.zeros_like(pet_data)
for t in range(pet_data.shape[-1]):
    positron_range_corrected_pet[..., t] =
apply_positron_range_correction(pet_data[..., t], POSITRON_RANGE_MM,
VOXEL_SIZE)

corrected_pet_data_prc =
spill_correction_volume(positron_range_corrected_pet, carotid_mask_4d,
VOXEL_SIZE, PSF_FWHM, num_iter=3, epsilon=1e-5)
```